11-2005

Geodetic GPS Measurements in South Iceland: Strain Accumulation and Partitioning in a Propagating Ridge System

P. C. LaFemina
University of Miami

Timothy H. Dixon
University of Miami, thd@usf.edu

R. Malservisi
University of Miami

T. Arnadottir
University of Iceland

E. Sturkell
University of Iceland

See next page for additional authors

Geodetic GPS measurements in south Iceland: Strain accumulation and partitioning in a propagating ridge system

P. C. LaFemina,[1] T. H. Dixon,[1] R. Malservisi,[1,2] T. Árnadóttir,[3] E. Sturkell,[3] F. Sigmundsson,[3] and P. Einarsson[4]

Received 7 February 2005; revised 20 May 2005; accepted 1 August 2005; published 18 November 2005.

[1] GPS observations in south Iceland between 1994 and 2003 are compared with two-dimensional elastic half-space and viscoelastic coupling models for two parallel rift zones, representing the Western and Eastern volcanic zones (WVZ, EVZ). GPS data from the Hreppar block, between the WVZ and EVZ, fit a rigid block model within uncertainties. Spreading rates across the WVZ increase from 2.6 ± 0.9 mm/yr in the northeast to 7.0 ± 0.4 mm/yr in the southwest. Conversely, spreading rates in the EVZ decrease from 19.0 ± 2.0 mm/yr in the northeast to 11.0 ± 0.8 mm/yr in the southwest, the direction of ridge propagation. Summed extension rates across the two rift zones are approximately constant and equal to the total plate rate, ~18–20 mm/yr, consistent with a simple propagating ridge model whereby the WVZ is deactivating in the direction of EVZ propagation. The coupling model confirms results from the simple elastic half-space model, including relatively shallow locking depths (<5 km) beneath the rift zones, and allows for an estimate of mean viscosity (~10^{19}–10^{20} Pa s) beneath the elastic layer. The location of maximum surface velocity gradient in the EVZ, presumably the locus of subsurface magma accumulation and future rifting, does not coincide with the 1783–1784 Lakagígar fissure eruption but is 20 km to the west, on the Bárðabunga-Veidivötn fissure swarm. This had a small volume eruption in 1862–1864 but a major eruption in 1477 A.D.

Citation: LaFemina, P. C., T. H. Dixon, R. Malservisi, T. Árnadóttir, E. Sturkell, F. Sigmundsson, and P. Einarsson (2005), Geodetic GPS measurements in south Iceland: Strain accumulation and partitioning in a propagating ridge system, *J. Geophys. Res.*, *110*, B11405, doi:10.1029/2005JB003675.

1. Introduction

[2] Short-term (less than ~1 Myr) extensional processes in the world's mid-ocean ridge system are difficult to observe and quantify due to their subaqueous setting. For slow spreading ridges in particular, the seafloor magnetic pattern, which accurately records the longer-term kinematics of extension, is not well resolved on shorter timescales. Rare subaerial exposures of the mid-ocean ridge in Iceland and Afar, both slow spreading, propagating ridges, allow detailed kinematic observations of the rifting process, including elastic strain accumulation and release associated with quasi-cyclic rifting via dike intrusion and associated fissure eruptions. Iceland additionally offers the opportunity to investigate ridge–hot spot interaction. In this paper we present detailed GPS observations across the Eastern and Western volcanic zones in south Iceland, part of the North America-Eurasia plate boundary zone. We compare our data to two-dimensional elastic half-space models and to a numerical viscoelastic coupling model that incorporates the first-order effects of the rifting cycle. We derive extension rate estimates for the Eastern and Western volcanic zones, assess spatial variations, and compare our results with geologic observations to assess some aspects of temporal evolution of this part of the mid-ocean ridge system.

2. Geologic Background

[3] Iceland is the subaerial exposure of the Mid-Atlantic Ridge (MAR), located between the Kolbeinsey Ridge to the north and the Reykjanes Ridge to the south (Figure 1). West-northwest motion of the MAR relative to the Iceland hot spot has resulted in repeated southeastward ridge jumps since ~23 Ma and formation of overlapping spreading centers [*Garcia et al.*, 2003; *Hardarson et al.*, 1997; *Oskarsson et al.*, 1985]. In southern Iceland, the MAR consists of two overlapping, subparallel ridge segments, the Western and Eastern volcanic zones, separated by the Hreppar block (Figure 1). The South Iceland Seismic Zone,

[1]Rosenstiel School of Marine and Atmospheric Sciences, University of Miami, Miami, Florida, USA.
[2]Now at Department of Geology and Environmental Sciences, Ludwig-Maximilians University, Munich, Germany.
[3]Nordic Volcanological Center, Institute of Earth Sciences, University of Iceland, Reykjavik, Iceland.
[4]Science Institute, University of Iceland, Reykjavik, Iceland.

0148-0227/05/2005JB003675$09.00

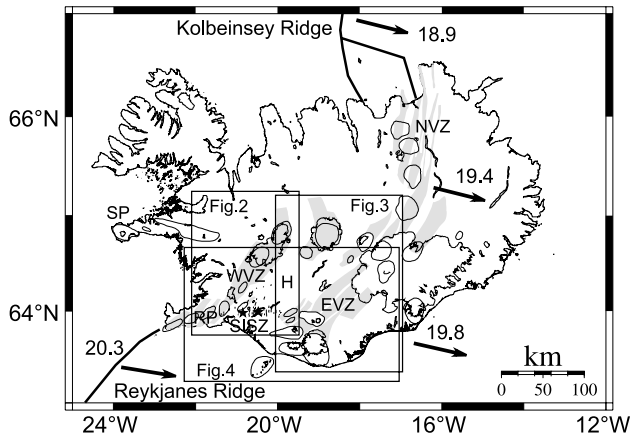

Figure 1. Neotectonic map of Iceland showing the central volcanoes (ellipses) and neovolcanic zones (gray): Northern Volcanic Zone (NVZ), Eastern Volcanic Zone (EVZ), Middle Volcanic Zone (MVZ), Western Volcanic Zone (WVZ) and Reykjanes Peninsula (RP) [*Einarsson and Saemundsson*, 1987]. The Snæfellsnes Peninsula (SP) was the location of the Mid-Atlantic Ridge prior to its east-southeast migration to the WVZ ~9 Ma. The South Iceland Seismic Zone (SISZ) is a transform zone connecting the WVZ and EVZ and was the location of two M_w 6.5 earthquakes on 17 and 21 June 2000 (stars). The Hreppar block (H) separates the WVZ and EVZ. Arrows show spreading directions and magnitudes (full rate) estimated from the REVEL plate motion model (rates in mm/yr) [*Sella et al.*, 2002]. Boxes indicate areas of Figures 2, 3, and 4.

an area of roughly north trending right-lateral strike-slip faults, accommodates left-lateral transform motion via "bookshelf" faulting, connecting the two ridge segments and the Reykjanes Peninsula (Figure 1) [*Einarsson*, 1991]. There is no equivalent seismically active transform boundary connecting the northern end of the Western Volcanic Zone with the Eastern Volcanic Zone. However, it has been proposed that this boundary acts as a leaky transform, accommodating relative plate motion during Quaternary time (Figure 1) [*Foulger et al.*, 2003; *Oskarsson et al.*, 1985]. One Holocene eruption has been documented there [*Kjartansson*, 1964].

[4] The Western Volcanic Zone (WVZ) has been active since ~7–9 Ma, when the ridge jumped eastward from the Snæfellsnes Peninsula [*Sæmundsson*, 1992]. The dominant trend of normal faults, fissures and dikes in the WVZ is ~N30°E [*Gudmundsson*, 1987]. The local extension direction is ~15° oblique to the NUVEL-1A plate motion model direction of 104° [*DeMets et al.*, 1994]. The width of the neovolcanic zone decreases from ~25 km at Langjökull (northern end) to ~15 km at Hengill volcano (southern end, and triple junction between Reykjanes Peninsula, South Iceland Seismic Zone and WVZ; Figure 2). In recent time, magmatic and tectonic activity has mainly occurred at the zone's southern end, including the eruption of Nesjahraun and the Sandey cinder cone in Lake Thingvallavatn at ~70 A.D., a possible rifting event in 1339, a rifting event without an eruption in 1789, and inflation and seismicity at Hengill volcano in 1993–1998 [*Gudmundsson*, 1987; *Sæmundsson*, 1992; *Sigmundsson et al.*, 1997; *Venzke et al.*, 2002]. However, Hallmundahraun erupted in ~925 A.D. from vents near Langjökull [*Jóhannesson*, 1989; *Venzke et al.*, 2002]. Thirty-five postglacial eruptions have been documented in the WVZ, including twelve in the Thingvellir Graben [*Sæmundsson*, 1992; J. Sinton, personal communication, 2005]. Geologic estimates of extension across the Thingvellir Graben, southern WVZ, indicate ~7.8–10.0 mm/yr spreading in the last 9 kyr, ~40–51% of the NUVEL-1A spreading rate of 18.4 mm/yr [*DeMets et al.*, 1994; *Gudmundsson*, 1987; *Sæmundsson*, 1992]. Subsidence in the Thingvellir graben has been measured geodetically and geologically at up to 7 mm/yr in postglacial time [*Tryggvason*, 1968].

[5] In contrast to these geologic estimates, geodetic data collected across the Thingvellir graben in the late 1960s and early 1970s have been interpreted to suggest slower spreading rates, 0–6.6 mm/yr, 0–34% of the NUVEL-1A rate [*Brander et al.*, 1976; *Decker et al.*, 1971, 1976; *Gerke*, 1974; *Sæmundsson*, 1992; *Sigmundsson et al.*, 1995;

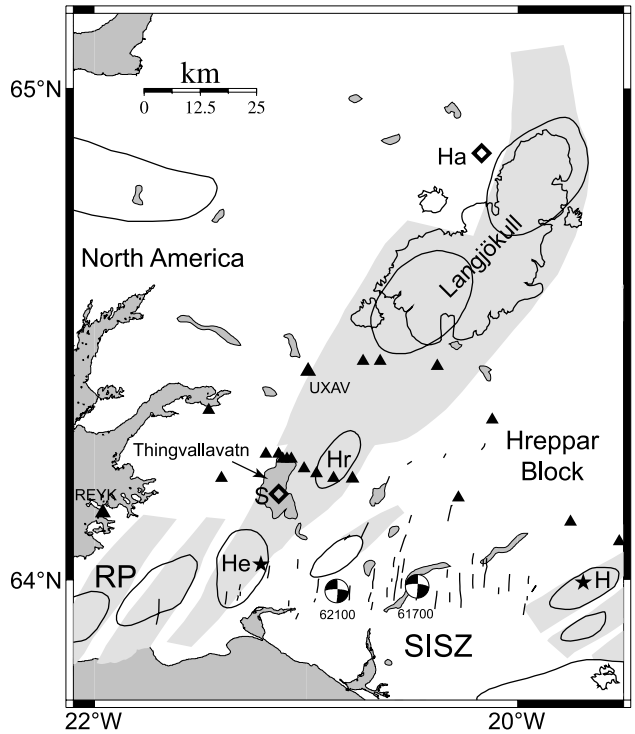

Figure 2. Western Volcanic Zone (WVZ) in relation to the South Iceland Seismic Zone (SISZ), Hreppar Block and Reykjanes Peninsula. Central volcanoes (ellipses), the main fissure swarms (gray), and glaciers (irregular borders) are also shown [*Einarsson and Saemundsson*, 1987]. Hengill volcano (He) is located at the triple junction of the WVZ, SISZ, and Reykjanes Peninsula and experienced an inflation episode between 1993 and 1998. Star denotes center of inflation estimated from InSAR data [*Feigl et al.*, 2000]. Focal mechanisms for the June 2000 SISZ earthquakes are from *Dziewonski et al.* [2001]. GPS site UXAV discussed in text is labeled. Triangles are GPS stations used in this study. Open diamonds are 70 A.D. Sandey (S) cinder cone and 925 A.D. Hallmundahraun (Ha) eruption locations. Lake Thingvallavatn and the central volcano Hrafnabjorg (Hr) are also shown.

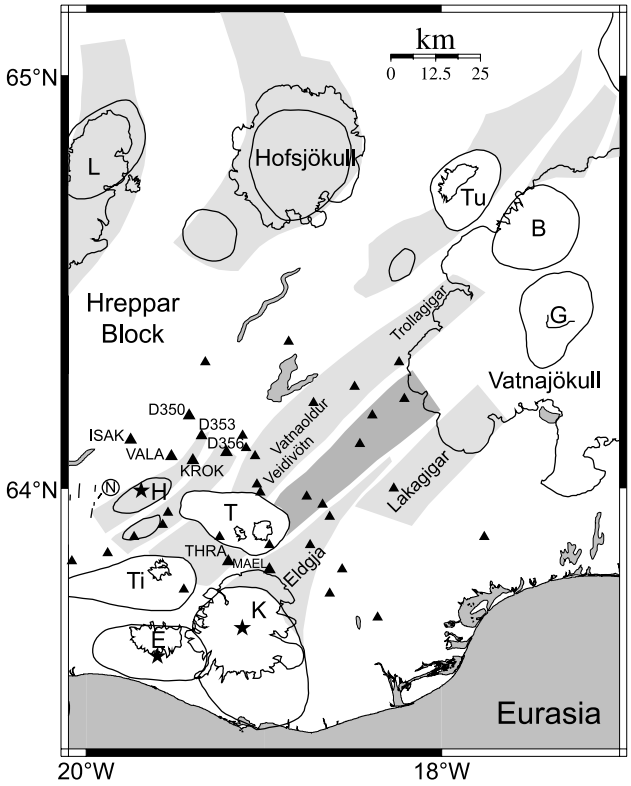

Figure 3. Map of Eastern Volcanic Zone (EVZ) with names and locations of historically active fissure swarms and central volcanoes. See Table 1 for historical fissure eruption data. Symbols are as in Figure 2. Central volcanoes Bárðabunga (B), Eyjafjallajökull (E), Grimsvötn (G), Hekla (H), Katla (K), Torfajökull (T), Tindfjallajökull (Ti), and Tungnafellsjökull (Tu) are shown. The darker gray zone is the location with no mapped Holocene volcanic activity [*Jóhannesson et al.*, 1990]. Triangles are GPS sites used in this study. GPS sites discussed in text are labeled. Stars indicate center of inflation at respective volcanoes [*Sigmundsson et al.*, 1992; *Sturkell et al.*, 2003a]. Næfurholt tilt station location marked by "N." Data from this station allow calculation of an independent deformation field for the 2000 eruption for correction of GPS site positions and velocities.

Tryggvason, 1982, 1990]. The low number of historical eruptions compared to the Eastern Volcanic Zone (see below), the eastward ridge jump, initiation of spreading and ridge propagation in the Eastern Volcanic Zone, and lack of a seismically active deformation zone connecting the northern limits of the Western and Eastern volcanic zones, have led some researchers to suggest that the WVZ is becoming inactive [*Einarsson*, 1991; *Oskarsson et al.*, 1985].

[6] The Eastern Volcanic Zone (EVZ) formed at ~2–3 Ma during the last eastward migration of spreading [*Sæmundsson*, 1974] and is propagating to the southwest at ~35–50 mm/yr [*Einarsson*, 1991]. The dominant trend of fissure swarms and dikes in the EVZ is N45°E (Figure 3). The extension direction here is ~30° oblique to the NUVEL-1A plate motion model direction. Holocene activity is restricted to two parallel ~15 km wide zones formed by overlapping fissures swarms associated with the central volcanoes Bárðarbunga, Torfajökull, and Hekla on the west side and Grimsvötn and Katla on the east side (Figure 3). A ~20 km wide zone with no mapped Holocene eruptive fissures separates the two zones [*Jóhannesson et al.*, 1990], and is considered inactive. Our new GPS results will show which of these zones is currently accumulating strain. Normal faulting is pervasive only in units greater than 0.7–3.1 Myr (i.e., at distances of ≥30 km from the geographic axis of the neovolcanic zone). The EVZ is currently aseismic [*Angelier et al.*, 2004; *Einarsson*, 1991; *Jóhannesson et al.*, 1990; *Lippitsch et al.*, 2005]; seismicity is restricted to active central volcanoes.

[7] There have been five historical fissure eruptions in the EVZ (Table 1), not including eruptions from Hekla and its associated fissure swarm. Postglacial eruptions are mainly from the central volcanoes, with more than 190 documented events [*Venzke et al.*, 2002].

3. Previous Work

[8] Geodetic GPS studies of crustal deformation in south Iceland have investigated rift-transform interactions [*Sigmundsson et al.*, 1995], strain accumulation and temporal variations in spreading within the EVZ [*Jónsson et al.*, 1997], strain accumulation and sinistral shear along the Reykjanes Peninsula [*Hreinsdóttir et al.*, 2001] and coseismic and postseismic deformation from the 17 and 21 June 2000 M_w6.5 South Iceland Seismic Zone (SISZ) earthquakes [*Árnadóttir et al.*, 2001, 2005, 2003]. *Sigmundsson et al.* [1995] concluded that the SISZ accommodates 85% ±15% of the full plate rate, or 15–21 mm/yr. This implies that divergence across the WVZ accommodates 15% ± 15% of the full plate rate or 0–6.3 mm/yr. *Jónsson et al.* [1997] analyzed GPS and electronic distance measurement (EDM) data across the EVZ, which suggest ~12 mm/yr of extension is accommodated in a zone 100 km wide. However, a comprehensive surface velocity field in a uniform reference frame spanning the entire deforming plate boundary zone has not been available prior to this study, complicating regional tectonic interpretations and assessment of strain partitioning between the neovolcanic zones.

4. Data Collection and Analysis

[9] Geodetic GPS studies have been conducted in Iceland since 1986 [*Einarsson et al.*, 1993]. We use data collected in 1994 and later, when GPS accuracy improved due to enhancements to the satellite constellation and the global tracking network. In 1965, EDM bench marks were installed and line lengths measured across the EVZ and WVZ

Table 1. Historical Rifting Episodes in the Eastern Volcanic Zone[a]

Fissure Swarm	Year	Time Since Last Event, years	Dike Thickness, m	Erupted Volume, km^3
Vatnaoldur	871 ± 2	-	?	3.3
Eldgja	934	63	?	19.3
Veidivötn	1477	536	10	9.1
Lakagígar	1783–1784	313	4.5	16.0
Trollagígar	1862–1764	81	1.5	0.3

[a]Note that erupted volumes are not dense rock equivalent (DRE) and are the sum of estimated tephra and lava volumes [*Jónsson et al.*, 1997; *Venzke et al.*, 2002].

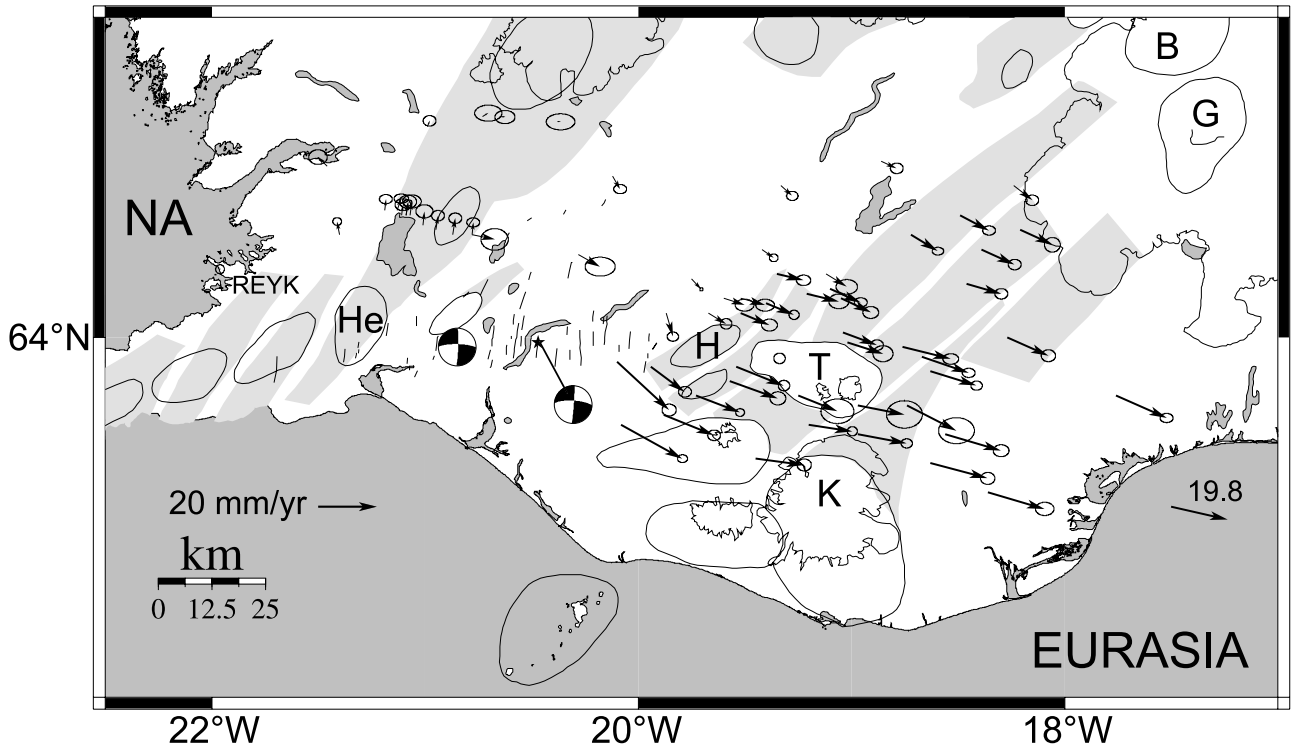

Figure 4. GPS-derived velocity field relative to stable North America for the period 1994–2003, not corrected for coseismic offsets or transient volcano deformation. Arrows indicate sites with complete seven to nine year time series. Black arrow located off the southeast coast is the predicted plate motion vector (19.8 mm yr^{-1}) from REVEL model [*Sella et al.*, 2002]. Note effects of coseismic deformation associated with the June 2000 earthquakes in the SISZ. In the WVZ site, vectors are deflected to the northeast and in the EVFZ site vectors have higher than expected velocities. Earthquake focal mechanisms for the 17 and 21 June 2000 earthquakes are from *Dziewonski et al.* [2001].

[*Decker et al.*, 1971]; these lines were reoccupied with GPS in 1994 and 1995, respectively [*Jónsson et al.*, 1997]. Other sites in the EVZ, WVZ and Hreppar block were also occupied during these surveys (Figure 4). Observation epochs were 16–22 hours during the 1994 and 1995 campaigns [*Jónsson et al.*, 1997]. In 2001 and 2003 we reoccupied every third site along the EVZ EDM line, and all other sites within the EVZ. Sites in the WVZ were reoccupied in 2003. Observation epochs for these campaigns consisted of a minimum of two full (24 hour) UTC days.

[10] All GPS data were reprocessed for this study, in order to generate an internally consistent velocity field with uniform analytical conditions and reference frame. The data were processed using GIPSY-OASIS version 2.5 [*Zumberge et al.*, 1997] following methods described by *Sella et al.* [2002], resulting in daily position estimates transformed into ITRF 1997 (Table 2) [*Boucher et al.*, 1999]. Mean uncertainties in daily position estimates for the 1995 and earlier data are ~9 mm in latitude, 12 mm in longitude and 26 mm in the vertical component. For the 2001 and 2003 data, daily position uncertainties are approximately 3 mm in latitude, 6 mm in longitude and 12 mm in the vertical component (unless noted, all uncertainties are quoted at one standard deviation). Site velocities are calculated using a linear regression through the daily position estimates. Velocity uncertainties are estimated using a model that accounts for the number and quality of observations, the total time span of measurements, and the presence of time-correlated ("colored") noise [*Mao et al.*, 1999]. Mean rate uncertainties are 1.0 mm/yr in latitude, 1.3 mm/yr in longitude and 2.5 mm/yr in the vertical component (Table 2). We calculated site velocities relative to stable North America, using the plate angular velocities of *Sella et al.* [2002](Figure 4).

[11] The measured (~decadal average) velocity field will be a good approximation to the secular (long term) velocity field associated with the interrifting period of strain accumulation provided that no additional processes operated during the observation period. As discussed below, this is clearly not the case, and additional steps are required to interpret the data.

5. Modeling the Site Velocities

[12] GPS-based site position or velocity estimates may be affected by a variety of processes, including secular plate motion, elastic and permanent deformation associated with current magmatic and tectonic events, and ongoing response to past events including rifting episodes and postglacial rebound. In order to use the velocity field to investigate the secular rifting signal, the effects of these additional processes must be accurately measured or modeled for each site, and the site position estimates and velocities recalculated accordingly. In addition to strain accumulation across the neovolcanic zones and SISZ, major geologic processes in South Iceland are believed to be (1) coseismic and

Table 2. GPS Velocities Relative to ITRF-97 and Weighted RMS Scatter, Not Corrected for Coseismic Offsets and Volcano Effects

					Velocity, mm yr^{-1}			WRMS, mm		
Site	Latitude	Longitude	ΔT	N	North	East	Vertical	North	East	Vertical
ALMA	64.25	−21.12	8.227	10	22.7 ± 0.4	−9.6 ± 1.3	−2.5 ± 2.3	2.0	6.8	11.2
BISK	64.24	−21.09	8.230	6	23.3 ± 0.9	−10.3 ± 0.9	−0.4 ± 1.5	4.0	4.5	4.7
BREI	64.18	−18.39	8.962	11	14.1 ± 0.8	1.2 ± 0.9	10.1 ± 2.3	4.5	5.3	13.1
BRSK	63.94	−19.54	9.014	16	12.5 ± 0.9	5.8 ± 0.9	4.2 ± 2.2	5.3	5.6	13.5
BULA	63.80	−18.55	8.934	8	13.8 ± 0.7	8.6 ± 0.9	4.7 ± 1.8	3.4	5.3	8.6
D350	64.18	−19.41	9.055	11	16.2 ± 0.8	−6.4 ± 1.2	7.3 ± 1.7	4.5	7.3	8.5
D353	64.12	−19.35	9.041	9	16.9 ± 0.7	−1.3 ± 0.8	8.0 ± 2.2	3.7	4.9	11.7
D356	64.09	−19.20	8.932	11	16.4 ± 0.9	0.6 ± 0.6	6.1 ± 2.1	4.6	3.5	11.5
D359	64.09	−19.10	9.079	13	14.3 ± 0.4	−0.2 ± 0.7	8.9 ± 2.4	2.2	4.3	14.4
D361	64.07	−19.04	8.962	10	14.3 ± 0.4	−0.1 ± 0.5	5.7 ± 1.8	2.2	3.3	8.5
D364	64.01	−19.04	9.096	12	14.8 ± 0.4	1.3 ± 0.9	3.7 ± 4.0	2.4	5.4	26.6
D365	63.99	−19.01	6.942	7	15.3 ± 1.5	1.9 ± 2.1	−0.1 ± 2.3	5.8	8.9	8.3
D369	63.97	−18.76	8.962	9	15.1 ± 0.3	6.2 ± 1.1	8.1 ± 3.0	1.3	6.1	17.0
D371	63.95	−18.66	8.964	12	13.7 ± 0.6	5.8 ± 0.5	6.0 ± 2.5	3.1	3.2	14.6
D372	63.92	−18.63	8.953	11	14.3 ± 0.8	5.6 ± 1.1	7.9 ± 2.5	4.0	6.3	14.1
DIMO	64.22	−20.95	8.205	6	23.6 ± 0.7	−10.1 ± 0.6	−2.3 ± 2.1	3.0	2.9	8.9
DROP	63.91	−19.57	6.940	7	13.1 ± 1.2	5.9 ± 1.1	7.8 ± 3.7	4.5	4.6	15.4
ELDH	63.68	−18.35	8.945	9	13.4 ± 0.5	7.9 ± 0.6	2.2 ± 2.3	2.3	3.4	12.4
FOSA	64.35	−21.46	4.104	7	21.7 ± 2.2	−14.1 ± 3.2	2.0 ± 5.3	5.2	8.2	13.4
GALT	63.99	−18.27	8.953	7	13.2 ± 1.2	4.1 ± 0.5	10.1 ± 3.5	5.7	2.8	19.3
GULL	64.32	−20.12	8.882	15	14.4 ± 1.0	−8.1 ± 1.1	7.9 ± 1.5	5.8	7.1	7.3
HGJA	64.25	−21.10	8.227	6	22.2 ± 0.7	−10.4 ± 0.8	−2.6 ± 1.9	3.2	3.8	7.3
ISAK	64.11	−19.74	9.288	130	15.4 ± 0.7	−7.2 ± 1.0	7.0 ± 2.4	5.8	9.3	24.2
JOKU	64.30	−18.24	7.068	7	14.6 ± 0.6	−2.3 ± 0.9	10.5 ± 2.1	2.2	4.1	7.5
KALK	63.92	−21.09	4.859	7	11.8 ± 1.3	16.2 ± 1.7	−0.7 ± 5.8	3.5	5.1	17.9
KARA	64.25	−21.18	8.208	6	22.6 ± 0.6	−10.4 ± 0.2	−1.4 ± 1.6	2.7	1.0	5.4
KELD	63.82	−20.08	8.000	18	5.3 ± 3.8	12.8 ± 4.3	2.0 ± 4.0	20.2	24.5	25.5
KGIL	63.85	−18.97	2.038	10	15.9 ± 1.0	5.0 ± 3.9	5.7 ± 9.2	1.3	5.8	13.1
KOPS	64.17	−20.27	4.019	6	14.6 ± 0.8	−3.4 ± 1.8	3.1 ± 2.6	1.8	4.6	4.0
KROK	64.06	−19.39	8.964	17	15.0 ± 1.0	−0.9 ± 1.0	5.4 ± 4.4	5.8	6.7	32.2
KVIS	64.20	−18.72	9.088	9	13.6 ± 0.5	−1.1 ± 0.7	11.0 ± 1.7	2.4	4.3	8.1
LAMH	64.44	−20.38	8.049	5	18.7 ± 1.7	−9.6 ± 0.9	1.8 ± 1.2	7.0	4.1	2.0
LANG	64.31	−19.33	9.159	10	15.6 ± 0.5	−6.6 ± 0.6	6.4 ± 2.0	2.4	3.6	10.9
LAUG	64.21	−20.78	8.107	6	23.0 ± 1.3	−10.4 ± 1.1	−0.7 ± 2.7	5.7	5.2	11.7
LAUV	64.21	−20.78	4.151	5	17.2 ± 0.5	−3.1 ± 2.4	−0.7 ± 3.7	1.0	5.9	7.6
LAVA	64.20	−20.86	8.203	6	24.3 ± 1.3	−9.8 ± 1.4	1.6 ± 2.4	5.7	6.7	10.2
LISA	64.21	−21.39	8.200	10	23.2 ± 1.0	−11.9 ± 0.7	−0.3 ± 2.4	4.8	3.7	12.0
LJOS	64.24	−18.48	9.090	9	14.0 ± 0.5	−0.3 ± 1.1	12.3 ± 1.8	2.6	6.2	8.6
MAEL	63.80	−18.96	7.937	13	16.2 ± 0.9	6.5 ± 0.7	7.5 ± 5.3	4.3	3.9	32.4
NLAN	64.22	−18.20	8.962	12	14.2 ± 1.0	0.9 ± 0.6	8.5 ± 1.6	5.2	3.7	8.0
OD17	64.12	−19.12	9.074	10	14.7 ± 0.6	−3.3 ± 0.5	6.1 ± 1.5	3.2	3.3	6.7
PALA	63.88	−19.72	9.019	17	12.9 ± 1.0	4.4 ± 1.0	2.2 ± 2.2	6.0	6.5	14.0
REYK	64.13	−21.95	7.716	2638	20.1 ± 0.4	−11.5 ± 0.4	−4.0 ± 1.0	3.7	4.2	8.5
SATU	63.88	−19.25	2.036	10	13.7 ± 3.5	3.0 ± 0.8	11.0 ± 5.7	4.8	1.5	6.4
SKHR	63.83	−19.88	7.932	17	11.6 ± 1.3	6.8 ± 1.3	3.1 ± 3.8	6.8	7.4	23.4
SKOT	64.22	−21.01	8.216	6	23.4 ± 0.6	−10.4 ± 0.5	−0.8 ± 2.2	2.4	2.7	9.5
SLAN	64.10	−18.45	8.959	11	15.8 ± 0.6	1.7 ± 0.7	3.6 ± 2.3	3.1	4.0	12.6
SNAE	63.73	−18.63	3.096	40	14.0 ± 0.8	9.4 ± 0.9	12.0 ± 3.3	1.9	2.7	6.9
STOB	64.44	−20.72	8.049	5	19.9 ± 1.7	−8.8 ± 1.4	0.2 ± 1.5	7.0	6.1	4.6
TEIG	63.88	−17.75	8.951	10	11.7 ± 0.8	7.2 ± 0.6	9.9 ± 2.8	4.1	3.8	16.5
THRA	63.82	−19.19	7.937	11	16.8 ± 0.8	4.5 ± 0.5	5.0 ± 3.1	4.0	2.8	16.5
THVE	63.86	−18.74	2.027	8	10.5 ± 1.4	6.7 ± 1.5	15.5 ± 7.9	1.7	2.3	10.0
TJAF	64.45	−20.64	8.044	7	18.7 ± 0.7	−9.1 ± 1.1	6.6 ± 1.9	3.2	5.2	7.3
UXAV	64.43	−20.98	8.049	7	20.7 ± 0.9	−10.1 ± 0.7	0.8 ± 3.7	4.0	3.5	18.5
VALA	64.07	−19.52	8.964	12	16.3 ± 1.5	−2.1 ± 2.0	8.9 ± 1.8	8.1	11.7	9.5
VATN	64.24	−21.09	8.230	19	22.9 ± 0.9	−10.3 ± 0.7	−1.5 ± 1.7	4.8	4.4	8.0
VAVI	64.24	−21.06	8.225	6	23.4 ± 0.4	−10.2 ± 0.7	−5.6 ± 1.6	1.5	3.6	5.5

postseismic deformation from the 17 and 21 June 2000 M_w6.5 SISZ earthquakes [*Árnadóttir et al.*, 2001, 2005; *Pedersen et al.*, 2003, 2001]; (2) deformation from the 28 February to 6 March 2000 Hekla eruption [*Sigmundsson and Einarsson*, 2000; *Sigmundsson et al.*, 2001]; (3) inflation and seismicity at Hengill volcano for the period 1993–1998 [*Feigl et al.*, 2000; *Sigmundsson et al.*, 1997]; (4) ongoing inflation/deflation at Eyjafjallajökull and Katla volcanoes [*Sturkell et al.*, 2003a]; and (5) postglacial rebound associated with Holocene deglaciation and recent glacial retreat [*Sigmundsson*, 1991; *Sigmundsson and Einarsson*, 1992]. We discuss below how these various strain sources are quantified, whether they affect the site positions, and if necessary, how the corresponding position time series are corrected. Because of data limitations, the volcanic corrections may have considerable uncertainty. In subsequent models, we therefore consider velocity fields both with and without the volcanic corrections. The uncor-

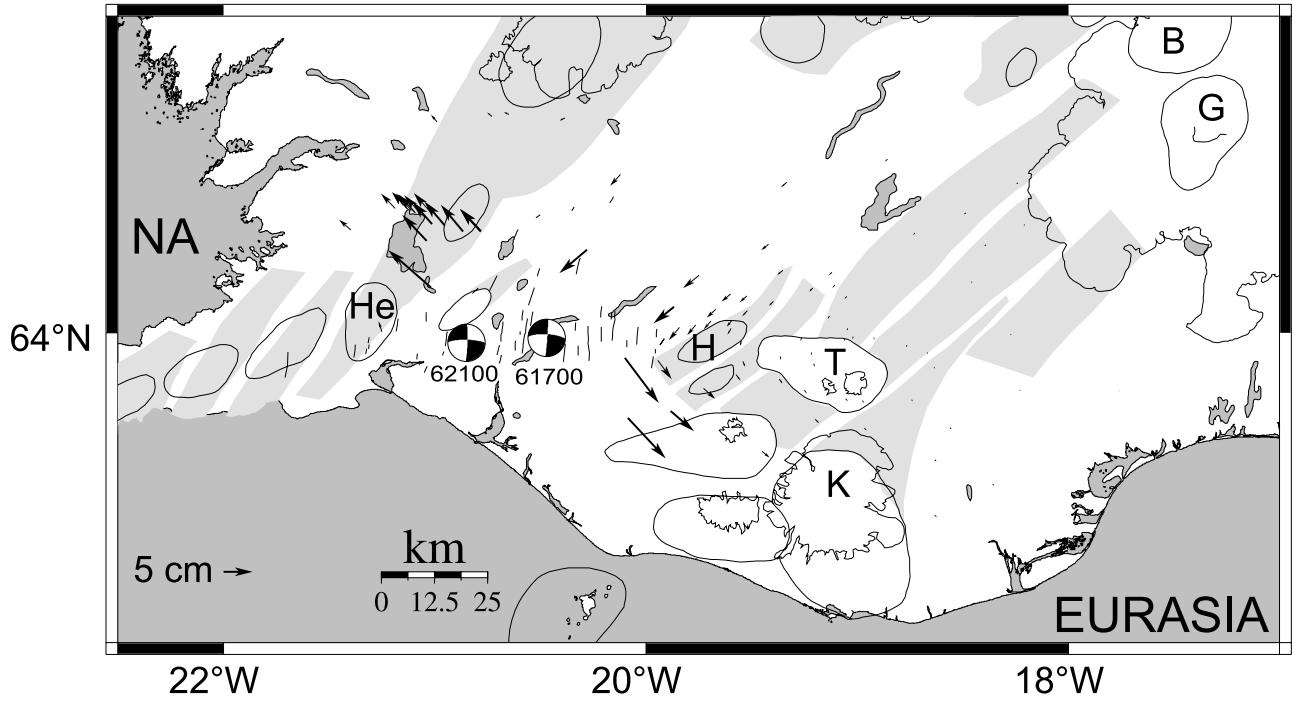

Figure 5. Coseismic displacements calculated at sites used in this study from the distributed slip model of *Pedersen et al.* [2003] for the June 2000 SISZ earthquakes. See Table 4 for offset components. Coseismic estimates are used to correct site positions; velocities are then recalculated. Corrected velocity field is presented in Figure 8 and Table 8.

rected position time series are listed by *LaFemina* [2005]. Since we are mainly interested in horizontal deformation, we do not correct our velocity field for vertical motion associated with postglacial rebound and historic retreat of the Vatnajökull glacier [*Sigmundsson*, 1991; *Sigmundsson and Einarsson*, 1992], that is, we assume that the horizontal component of deformation associated with these processes is negligible.

5.1. The 17 and 21 June 2000 SISZ Earthquakes

[13] The 17 and 21 June 2000 M_w6.5 earthquakes and triggered seismicity ended a quiet period in the SISZ dating back to 1912 [*Árnadóttir et al.*, 2001; *Pagli et al.*, 2003; *Pedersen et al.*, 2003, 2001]. We omitted sites within 20 km of the earthquake epicenters from this study, where coseismic offsets are large. For remaining sites, we calculated coseismic offsets predicted by the distributed slip model of *Pedersen et al.* [2003] on the basis of interferometric synthetic aperture radar (InSAR) and local GPS observations (Figure 5 and Table 3). Site position estimates were corrected for epochs after 21 June 2000 and velocities recalculated accordingly. *Árnadóttir et al.* [2005] investigated postseismic transient deformation following the June 2000 earthquakes and determined that any signal associated with afterslip on the fault planes or viscoelastic relaxation in the lower crust and upper mantle decayed rapidly after 2001.

5.2. The 2000 Hekla Eruption

[14] Hekla volcano is located at the intersection of the SISZ and EVZ and has erupted 7 times in the last century, including four eruptions in the last 34 years. Position time series of sites located in the Hekla network indicate inflation of the volcano after the 1991 eruption, followed by rapid deflation during and reinflation after the 28 February to 6 March 2000 eruption. Tilt measurements have been made at Hekla volcano since 1968 [*Tryggvason*, 1968]. The east component of tilt measured at station Næfurholt, 11.5 km west of the center of the eruptive fissure, mainly reflects displacement caused by a deep-seated magma chamber (Figures 3 and 6). This radial tilt component indicates inflation prior to the 1991 and 2000 eruptions, and rapid deflation during the eruptions (Figure 6). The net amount of tilt measured at Næfurholt between 1994 and 2003, the period of our GPS time series, is 2.5 μrad. The magma chamber at Hekla has been estimated geodetically to be between 6 and 11 km depth [*Linde et al.*, 1993; *Sigmundsson and Einarsson*, 1992; *Sigmundsson et al.*, 1992; *Tryggvason*, 1994] for several eruptions. The most recent estimate based on reinterpretation of borehole strain data following the February 2000 eruption places the magma chamber at 11 km depth (K. Ágústsson, personal communication, 2004).

[15] We estimate deformation at Hekla volcano using a Mogi point source model for deformation caused by a pressure or volume change in an elastic half-space [*Mogi*, 1958]. We assume that the depth of the source (magma chamber) is 11 km, that the horizontal location of the magma chamber is the middle of the eruptive fissure (star at Hekla volcano in Figure 3), and that the source produces a tilt signal of 2.5 μrad 11.5 km from the source. We then apply this result to calculate displacement and rate components for nearby sites (Table 4 and Figure 7). The calculations show that at a distance of 24 km, the radial component of displacement between 1994 and 2003 is ~9 mm, or 1 mm/yr, the approximate level of our rate uncertainty for this time period. Position estimates for sites

Table 3. Coseismic Displacements Calculated at Sites Used in This Study Using the Model of *Pedersen et al.* [2003]

Site	East, m	North, m	Vertical, m
ALMA	−0.0262	0.0284	−0.0071
BISK	−0.0280	0.0307	−0.0074
BREI	−0.0023	−0.0023	0.0008
BRSK	0.0040	−0.0097	−0.0009
BULA	0.0022	−0.0026	−0.0007
D350	−0.0129	−0.0103	0.0034
D353	−0.0100	−0.0083	0.0026
D356	−0.0061	−0.0060	0.0016
D359	−0.0050	−0.0051	0.0014
D361	−0.0039	−0.0045	0.0011
D364	−0.0016	−0.0042	0.0004
D365	−0.0009	−0.0040	0.0002
D369	−0.0002	−0.0030	0.0001
D371	0.0001	−0.0027	−0.0000
D372	0.0006	−0.0026	−0.0002
DIMO	−0.0354	0.0418	−0.0082
DROP	0.0083	−0.0110	−0.0018
ELDH	0.0025	−0.0024	−0.0009
FOSA	−0.0129	0.0130	−0.0042
GALT	−0.0004	−0.0018	0.0001
GULL	−0.0177	−0.0194	0.0048
HGJA	−0.0270	0.0295	−0.0073
ISAK	−0.0278	−0.0221	0.0054
JOKU	−0.0026	−0.0022	0.0009
KALK	−0.0055	−0.0045	0.0018
KARA	−0.0246	0.0256	−0.0068
KELD	0.0653	−0.0699	−0.0079
KGIL	0.0032	−0.0041	−0.0010
KOPS	−0.0481	−0.0407	0.0065
KROK	−0.0079	−0.0080	0.0019
KVIS	−0.0040	−0.0034	0.0012
LAMH	−0.0087	−0.0045	0.0013
LANG	−0.0105	−0.0090	0.0032
LAUG	−0.0356	0.0382	−0.0064
LAUV	−0.0357	0.0384	−0.0064
LAVA	−0.0383	0.0460	−0.0079
LISA	−0.0201	0.0177	−0.0054
LJOS	−0.0031	−0.0027	0.0010
MAEL	0.0044	−0.0044	−0.0013
NLAN	−0.0021	−0.0020	0.0007
OD17	−0.0060	−0.0054	0.0017
PALA	0.0202	−0.0182	−0.0037
REYK	−0.0053	0.0052	−0.0016
SATU	0.0049	−0.0061	−0.0013
SKHR	0.0407	−0.0351	−0.0067
SKOT	−0.0341	0.0388	−0.0082
SLAN	−0.0018	−0.0023	0.0006
SNAE	0.0032	−0.0031	−0.0011
STOB	−0.0086	0.0067	−0.0017
TEIG	0.0004	−0.0012	−0.0001
THRA	0.0065	−0.0062	−0.0018
THVE	0.0020	−0.0031	−0.0006
TJAF	−0.0082	0.0042	−0.0011
UXAV	−0.0105	0.0125	−0.0035
VALA	−0.0122	−0.0108	0.0027
VATN	−0.0282	0.0310	−0.0075
VAVI	−0.0290	0.0324	−0.0076

within 24 km of Hekla were corrected accordingly and velocities recalculated for the period 1994–2003.

5.3. The 1993–1998 Hengill Inflation

[16] Hengill central volcano experienced rapid inflation and seismic swarms in the period 1993–1998. Deformation studies during this period measured up to 19 mm/yr of inflation centered on Hrómundartindur volcano, southeast of Hengill (Figure 2) [*Feigl et al.*, 2000; *Sigmundsson et al.*, 1997]. We estimate the maximum amount of deformation at sites along our profile using the source location, depth, and maximum displacement above the source of *Feigl et al.* [2000] (Table 5). The maximum radial component of deformation at sites along profile 2 was less than 1.5 mm/yr. Our time series for sites in the area are based on measurements in 1995 and 2003. Time series are corrected for the corresponding 3-year period (1995–1998) of deformation, assuming the rate of deformation was constant and permanent. The latter assumption is suggested by time series from continuous GPS sites in the area (H. Geirsson et al., Current plate movements across the Mid-Atlantic Ridge determined from 5 years of continuous GPS measurements in Iceland, submitted to *Journal of Geophysical Research*, 2005).

5.4. Katla and Eyjafjallajökull Volcanoes

[17] Katla and Eyjafjallajökull volcanoes have both experienced inflation episodes during the period of our GPS observations [*Sturkell et al.*, 2003a]. Katla is a subglacial volcano, covered by the Myrdalsjökull icecap, and has had only one recent large eruption, in 1918. Geodetic observations at Katla between 1993 and 2000 indicate a total uplift

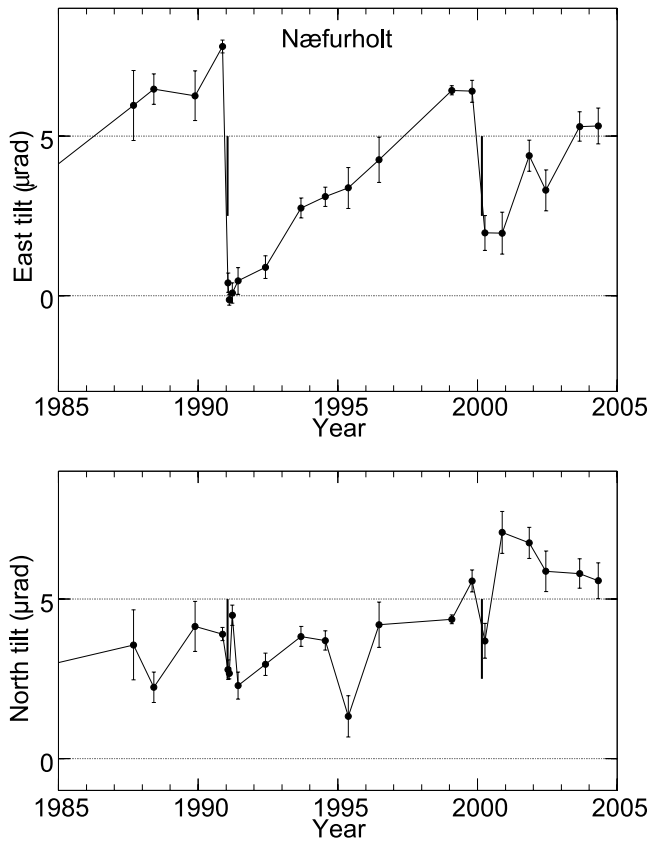

Figure 6. Time series of tilt measurements in the north and east components from site Næfurholt located 11.5 km west of Hekla volcano (Figure 3; circled N). Error bars are 1-sigma uncertainties. The east component is assumed to be the radial tilt component and is used to calculate the displacement of sites along profiles 2 and 3. See Table 5 for site displacements used to correct for Hekla reinflation following the February 2000 eruption. Vertical black lines mark the 1991 and 2000 eruptions.

Table 4. Site Displacements and Rates for the Period 1994 to 2003 for Sites Along Profiles 2 and 3 Due to Hekla Deformation Preceding and Following the February 2000 Eruption

	Displacement, m		Rate, mm/yr	
Site	East	North	East	North
BRSK	0.0183	−0.0104	2.0	−1.2
D350	0.0040	0.0064	0.4	0.7
D353	0.0067	0.0072	0.7	0.8
D356	0.0066	0.0034	0.7	0.4
DROP	0.0129	−0.0158	1.4	−1.8
ISAK	−0.0044	0.0154	−0.5	1.7
KELD	−0.0057	−0.0054	−0.6	−0.6
KROK	0.0125	0.0081	1.4	0.9
PALA	−0.0025	−0.0193	−0.3	−2.1
SKHR	−0.0064	−0.0113	−0.7	−1.3
SKJA	0.0075	0.0169	0.8	1.9
THJO	−0.0141	0.0132	−1.6	1.5
VALA	0.0102	0.0130	1.1	1.4

of 12 cm; measurements between 2000 and 2003 indicate inflation of ~2 cm/yr [*Sturkell et al.*, 2003a, 2003b]. We use the source location, depth, and maximum displacement above the source of *Sturkell et al.* [2003a] to calculate the influence of Katla inflation at nearby sites. Only two sites, THRA and MAEL, are affected above the millimeter per year level during the 2000 to 2003 period (Table 6 and Figure 3). The position estimates for epochs between 2000 and 2003 are corrected for the modeled horizontal displacements and the time series recalculated.

[18] Geodetic and seismic data suggest that Eyjafjallajökull experienced inflation episodes in 1994 and 1999 [*Pedersen and Sigmundsson*, 2004; *Sturkell et al.*, 2003a]. *Pedersen and Sigmundsson* [2004] fit a sill model to InSAR displacement data covering the 1994 deformation and seismic episode. The deformation field indicates surface displacements to the south-southeast. *Sturkell et al.* [2003a] use geodetic GPS and tilt measurements to investigate the 1999 deformation episode. The 1999 deformation field is similar in areal extent and magnitude to that in 1994, suggesting a similar source (i.e., a sill). However, *Sturkell et al.* [2003a] fit the data well with a Mogi source model; we adopt this model here. The two models are similar in terms

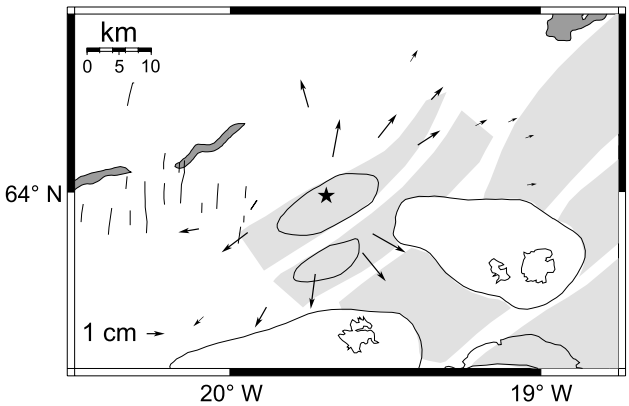

Figure 7. Displacement field for the 28 February to 6 March 2000 eruption of Hekla volcano, calculated from tilt data from site Næfurholt (N, Figure 3) and estimates of magma chamber depth from local borehole strain meter data.

Table 5. Components of Displacement and Rate for the Period 1993 to 1998 for Sites Along Profile 2 Due to Inflation of Hengill Volcano[a]

	Displacement, m		Rate, mm/yr	
Site	East	North	East	North
ALMA	0.0006	0.0037	0.2	1.2
BISK	0.0009	0.0038	0.3	1.2
DIMO	0.0021	0.0035	0.7	1.1
HGJA	0.0008	0.0039	0.2	1.3
KARA	0.0001	0.0038	0.0	1.2
LAUG	0.0022	0.0021	0.7	0.7
LAVA	0.0024	0.0028	0.8	0.9
LISA	−0.0020	0.0047	−0.6	1.5
SKOT	0.0016	0.0037	0.5	1.2

[a]See *Feigl et al.* [2000].

of the predicted far-field displacements, where our sites are located.

6. Secular Velocity Field for South Iceland

[19] The residual velocity field after application of the coseismic corrections is listed in Tables 7 and 8 and shown relative to stable North America in Figure 8. It may be considered an approximation to the secular velocity field for South Iceland during an interrifting period. Sites west of the WVZ have velocities consistent with a location on stable North America, while sites east of the EVZ have velocities consistent with a location on stable Eurasia. Sites located on the Hreppar block, between the EVZ and WVZ, have velocities that are intermediate in rate and approximately parallel to the plate motion direction, and thus show no evidence of internal deformation of the block within uncertainties.

[20] Inspection of the surface velocity field accounting for coseismic offsets and local volcanic deformation confirms that secular spreading across the rift zones and associated elastic strain accumulation are the dominant residual signals. Most site velocity vectors are parallel to the overall plate motion direction, and their amplitude (rate) increases with increasing distance from the adjacent plate and main rift zones. This is apparent in the stable North America reference frame (Figure 8). This suggests that it is appropriate to consider simple two-dimensional dike models and velocity profiles, using the component of velocity that is parallel to the plate motion direction. We therefore define three profiles spanning the EVZ and WVZ (Figure 8). Only sites located within 10 km of a profile are used (total profile width is 20 km). The component of velocity parallel to the REVEL plate motion direction, 102° [*Sella et al.*, 2002] is calculated. Profile 1 (northern profile) consists of sites south of Vatnajökull in the EVZ, on the Hreppar block, and a line

Table 6. Site Displacements and Rates for the Period 2000 to 2003 for Sites THRA and MAEL Along Profile 3 Due to Katla Deformation[a]

	Displacement, m		Rate, mm/yr	
Site	East	North	East	North
MAEL	0.0017	0.0037	0.5	1.2
THRA	−0.0008	0.0036	−0.2	1.2

[a]See *Sturkell et al.* [2003a].

Table 7. GPS Velocities Relative to ITRF-97 and Weighted RMS Scatter, Corrected for Coseismic Offsets but Not Corrected for Volcanic Effects[a]

					Velocity, mm yr^{-1}			WRMS, mm		
Site	Latitude	Longitude	ΔT	N	North	East	Vertical	North	East	Vertical
ALMA	64.25	−21.12	8.227	10	19.2 ± 0.4	−6.4 ± 1.2	−3.3 ± 2.3	2.0	6.7	11.2
BISK	64.24	−21.09	8.230	6	19.5 ± 0.9	−6.9 ± 0.9	−1.3 ± 1.5	4.0	4.5	4.7
BREI	64.18	−18.39	8.962	11	14.3 ± 0.9	1.4 ± 0.9	10.2 ± 2.3	4.7	5.5	13.0
BRSK	63.94	−19.54	9.014	16	13.4 ± 1.5	5.3 ± 0.9	4.1 ± 2.2	8.8	6.0	13.6
BULA	63.80	−18.55	8.934	10	12.9 ± 3.1	4.9 ± 8.9	5.0 ± 1.9	16.7	49.9	9.2
D350	64.18	−19.41	9.055	11	17.5 ± 0.7	−4.7 ± 1.1	7.7 ± 1.7	3.8	6.5	8.4
D353	64.12	−19.35	9.041	9	17.8 ± 0.6	−0.3 ± 0.8	8.3 ± 2.2	3.2	4.6	11.8
D356	64.09	−19.20	8.932	11	16.9 ± 0.9	1.1 ± 0.6	6.3 ± 2.1	4.7	3.5	11.4
D359	64.09	−19.10	9.079	13	14.9 ± 0.4	0.3 ± 0.6	9.0 ± 2.4	2.2	4.1	14.3
D361	64.07	−19.04	8.962	10	14.7 ± 0.5	0.2 ± 0.6	5.8 ± 1.8	2.4	3.4	8.5
D364	64.01	−19.04	9.096	12	15.3 ± 0.4	1.5 ± 0.9	3.8 ± 4.0	2.4	5.3	26.6
D365	63.99	−19.01	6.942	7	15.9 ± 1.5	2.0 ± 2.1	−0.1 ± 2.3	5.8	8.9	8.3
D369	63.97	−18.76	8.962	9	15.4 ± 0.3	6.2 ± 1.1	8.1 ± 3.0	1.2	6.1	17.0
D371	63.95	−18.66	8.964	6	14.0 ± 0.6	5.7 ± 0.6	6.0 ± 3.1	3.0	3.5	16.0
D372	63.92	−18.63	8.953	11	14.5 ± 0.8	5.5 ± 1.1	7.9 ± 2.5	4.3	6.3	14.1
DIMO	64.22	−20.95	8.205	6	18.5 ± 0.7	−5.8 ± 0.6	−3.3 ± 2.1	3.0	2.9	8.9
DROP	63.91	−19.57	6.940	7	14.7 ± 1.1	4.7 ± 1.2	7.6 ± 3.7	4.4	5.2	15.4
ELDH	63.68	−18.35	8.945	12	14.8 ± 1.4	13.4 ± 4.3	−2.4 ± 4.6	7.5	25.3	30.9
FOSA	64.35	−21.46	4.104	7	18.5 ± 2.2	−11.0 ± 3.1	1.0 ± 5.3	5.2	8.1	13.4
GALT	63.99	−18.27	8.953	3	14.1 ± 0.1	4.2 ± 0.1	9.0 ± 1.6	0.1	0.7	5.3
GULL	64.32	−20.12	8.882	15	17.1 ± 0.6	−5.7 ± 1.2	8.6 ± 1.5	3.3	7.3	6.9
HGJA	64.25	−21.10	8.227	6	18.6 ± 0.7	−7.2 ± 0.8	−3.5 ± 1.9	3.2	3.8	7.3
ISAK	64.11	−19.74	9.288	125	17.9 ± 0.4	−3.8 ± 0.6	7.7 ± 2.3	3.2	5.9	23.1
JOKU	64.30	−18.24	7.068	26	14.9 ± 0.5	−3.7 ± 1.2	12.6 ± 7.6	2.4	6.8	50.9
KALK	64.35	−18.85	7.058	7	17.3 ± 0.9	−4.2 ± 0.5	12.7 ± 2.9	3.7	2.2	11.5
KARA	64.25	−21.18	8.208	6	19.4 ± 0.6	−7.4 ± 0.2	−2.2 ± 1.6	2.7	1.0	5.4
KELD	63.82	−20.08	8.000	18	15.8 ± 1.1	3.0 ± 1.4	0.7 ± 4.1	5.6	8.5	26.2
KGIL	63.85	−18.97	2.038	10	15.9 ± 1.0	5.0 ± 3.9	5.7 ± 9.2	1.3	5.8	13.1
KOPS	64.17	−20.27	4.019	6	14.6 ± 0.8	−3.4 ± 1.8	3.1 ± 2.6	1.8	4.6	4.0
KROK	64.06	−19.39	8.964	17	15.9 ± 0.8	0.1 ± 0.9	5.7 ± 4.4	4.8	5.9	32.4
KVIS	64.20	−18.72	9.088	9	14.0 ± 0.5	−0.6 ± 0.7	11.1 ± 1.7	2.7	4.1	8.1
LAMH	64.44	−20.38	8.049	5	19.2 ± 1.7	−8.5 ± 0.9	2.0 ± 1.2	7.0	4.1	2.0
LANG	64.31	−19.33	9.159	10	16.7 ± 0.5	−5.3 ± 0.7	6.8 ± 2.1	2.4	4.0	11.1
LAUG	64.21	−20.78	8.211	12	18.3 ± 2.3	−5.9 ± 3.8	−1.4 ± 5.4	11.6	20.5	33.5
LAUV	64.21	−20.78	4.151	5	17.2 ± 0.5	−3.1 ± 2.4	−0.7 ± 3.7	1.0	5.9	7.6
LAVA	64.20	−20.86	8.203	6	18.7 ± 1.3	−5.2 ± 1.4	0.6 ± 2.4	5.7	6.7	10.3
LISA	64.21	−21.39	8.200	10	21.0 ± 0.7	−9.3 ± 0.8	−1.0 ± 2.6	3.5	4.4	13.1
LJOS	64.24	−18.48	9.090	9	14.3 ± 0.5	0.0 ± 1.1	12.4 ± 1.8	2.6	6.1	8.5
MAEL	63.80	−18.96	7.937	13	16.7 ± 1.0	6.0 ± 0.8	7.3 ± 5.3	4.9	4.3	32.3
NLAN	64.22	−18.20	8.962	12	14.4 ± 1.0	1.1 ± 0.6	8.5 ± 1.6	5.4	3.7	8.0
OD17	64.12	−19.12	9.074	9	15.1 ± 0.6	−3.0 ± 0.5	6.3 ± 1.5	3.3	2.9	6.5
PALA	63.88	−19.72	9.019	17	15.3 ± 1.1	1.7 ± 0.9	1.7 ± 2.3	6.3	5.8	14.5
REYK	64.13	−21.95	7.358	191	18.5 ± 0.4	−11.5 ± 0.5	−7.3 ± 1.5	2.6	4.0	9.9
SATU	63.88	−19.25	2.036	10	13.7 ± 3.5	3.0 ± 0.8	11.0 ± 5.7	4.8	1.5	6.4
SKHR	63.83	−19.88	7.932	17	15.8 ± 1.1	1.7 ± 1.2	2.3 ± 3.8	5.9	6.7	23.7
SKOT	64.22	−21.01	8.216	6	18.7 ± 0.6	−6.3 ± 0.5	−1.8 ± 2.2	2.4	2.7	9.5
SLAN	64.10	−18.45	8.959	11	16.0 ± 0.6	1.9 ± 0.7	3.6 ± 2.3	3.3	4.0	12.6
SNAE	63.73	−18.63	3.096	40	14.0 ± 0.8	9.4 ± 0.9	12.0 ± 3.3	1.9	2.7	6.9
STOB	64.44	−20.72	8.049	5	19.1 ± 1.7	−7.8 ± 1.4	0.0 ± 1.5	7.0	6.1	4.6
TEIG	63.88	−17.75	8.951	10	11.9 ± 0.8	7.2 ± 0.6	9.9 ± 2.8	4.2	3.8	16.5
THRA	63.82	−19.19	7.937	11	17.5 ± 1.0	3.7 ± 0.6	4.8 ± 3.1	4.7	3.3	16.4
THVE	63.86	−18.74	2.027	8	10.5 ± 1.4	6.7 ± 1.5	15.5 ± 7.9	1.7	2.3	10.0
TJAF	64.45	−20.64	8.044	7	18.2 ± 0.7	−7.7 ± 1.2	6.4 ± 1.9	2.9	6.0	7.4
UXAV	64.43	−20.98	8.049	7	19.1 ± 1.1	−8.8 ± 0.6	0.4 ± 3.6	5.0	3.0	17.7
VALA	64.07	−19.52	8.964	12	17.3 ± 1.3	−1.1 ± 1.8	9.1 ± 1.9	7.0	10.8	9.7
VATN	64.24	−21.09	8.230	19	19.3 ± 0.9	−6.8 ± 0.7	−2.4 ± 1.6	5.0	4.7	7.7
VAVI	64.24	−21.06	8.225	6	19.4 ± 0.4	−6.7 ± 0.7	−6.6 ± 1.6	1.5	3.6	5.5

[a]Site velocities in Table 8 were corrected for coseismic displacements following the 17 and 21 June 2000 SISZ earthquakes. Sites corrected for volcanic effects are listed in Tables 4, 5, and 6.

of sites south of Langjökull in the WVZ (Figures 8 and 9a). Profile 2 (central profile) consists of sites located along the WVZ and EVZ EDM lines, just north of the SISZ, on the Hreppar block, and outside the neovolcanic zones (Figures 8 and 9b). Profile 3 (southern profile) spans the Eastern Volcanic Flank Zone, north of Myrdalsjökull and south of Torfajökull (Figures 8 and 9c).

[21] Inspection of profiles 1 through 3 (Figures 9a–9c), gives an indication of the location of maximum velocity gradient and width of active strain accumulation for both neovolcanic zones. For the WVZ, profiles 1 and 2 indicate a decrease in width of strain accumulation from ~35 km in the north to ~25 km in south. Along both profiles the maximum velocity gradient is located along the western

Table 8. GPS Velocities Relative to Stable North America and Corrected for Coseismic Offsets Following the 17 and 21 June 2000 SISZ Earthquakes

	Velocity, mm yr^{-1}	
Site	North	East
ALMA	0.51 ± 0.45	4.54 ± 1.20
BISK	0.80 ± 0.90	4.03 ± 0.92
BREI	−4.93 ± 0.90	11.52 ± 0.92
BRSK	−5.61 ± 0.90	15.75 ± 1.51
BULA	−5.60 ± 0.83	18.64 ± 1.30
D350	−1.53 ± 0.73	5.73 ± 1.10
D353	−1.24 ± 0.64	10.10 ± 0.80
D356	−2.17 ± 0.61	11.46 ± 0.92
D359	−4.19 ± 0.45	10.63 ± 0.61
D361	−4.40 ± 0.54	10.51 ± 0.61
D364	−3.80 ± 0.45	11.80 ± 0.90
D365	−3.21 ± 1.51	12.29 ± 2.1
D369	−3.76 ± 0.37	16.42 ± 1.1
D371	−5.18 ± 0.61	15.89 ± 0.64
D372	−4.68 ± 0.83	15.67 ± 1.10
DIMO	−0.23 ± 0.61	5.08 ± 0.73
DROP	−4.30 ± 1.12	15.15 ± 1.20
ELDH	−5.63 ± 0.45	17.77 ± 0.61
FOSA	−0.12 ± 2.21	0.04 ± 3.10
GALT	−5.95 ± 0.51	14.17 ± 1.22
GULL	−1.79 ± 0.64	4.95 ± 1.20
HGJA	−0.09 ± 0.73	3.73 ± 0.80
ISAK	−1.07 ± 0.45	6.72 ± 0.61
JOKU	−4.36 ± 0.54	6.38 ± 1.20
KALK	−1.84 ± 0.51	6.07 ± 0.92
KARA	0.72 ± 0.22	3.55 ± 0.64
KELD	−3.10 ± 1.12	13.60 ± 1.40
KGIL	−3.22 ± 1.02	15.27 ± 3.90
KOPS	−4.26 ± 0.83	7.28 ± 1.80
KROK	−3.14 ± 0.83	10.51 ± 0.90
KVIS	−5.16 ± 0.54	9.62 ± 0.71
LAMH	0.36 ± 0.90	2.23 ± 1.71
LANG	−2.35 ± 0.54	5.11 ± 0.71
LAUG	−0.46 ± 2.31	4.93 ± 3.80
LAUV	−1.56 ± 0.54	7.73 ± 2.40
LAVA	−0.04 ± 1.32	5.66 ± 1.40
LISA	2.36 ± 0.73	1.71 ± 0.80
LJOS	−4.91 ± 0.54	10.15 ± 1.10
MAEL	−2.42 ± 0.80	16.26 ± 1.02
NLAN	−4.86 ± 0.61	11.17 ± 1.02
OD17	−3.99 ± 0.51	7.33 ± 0.64
PALA	−3.67 ± 0.90	12.20 ± 1.12
REYK	−0.82 ± 0.13	−0.03 ± 0.23
SATU	−5.36 ± 0.80	13.36 ± 3.51
SKHR	−3.14 ± 1.12	12.24 ± 1.20
SKOT	−0.01 ± 0.51	4.60 ± 0.64
SLAN	−3.22 ± 0.64	12.03 ± 0.71
SNAE	−5.18 ± 0.83	19.56 ± 0.90
STOB	0.33 ± 1.40	3.03 ± 1.71
TEIG	−7.44 ± 0.61	17.11 ± 0.83
THRA	−1.57 ± 0.61	14.04 ± 1.02
THVE	−8.66 ± 1.42	16.90 ± 1.50
TJAF	−0.59 ± 0.73	3.11 ± 1.20
UXAV	0.38 ± 0.61	2.11 ± 1.12
VALA	−1.71 ± 1.32	9.35 ± 1.80
VATN	0.60 ± 0.71	4.13 ± 0.92
VAVI	0.70 ± 0.45	4.22 ± 0.71

edge of the neovolcanic zone. For the EVZ, the zone of strain accumulation spans a wider area. Profiles 1 and 2 indicate a roughly 100 km wide area of strain accumulation. Profile 3 indicates a narrower zone of ~70 km across the Eastern Volcanic Flank Zone. The location of maximum velocity gradient appears to be consistent from north to south and is located on the eastern edge of the Veidivötn-Bárðarbunga fissure swarm and its extension south of Torfajökull volcano (profile 3).

7. Elastic Dislocation Model

[22] Geologic investigations of central volcanoes and neovolcanic zones in Iceland indicate that plate motion is accommodated by repeated, lateral dike injection [*Gudmundsson*, 2000; *Sigurdsson and Sparks*, 1978; *Walker*, 1960]. To investigate how long-term spreading across the Mid-Atlantic Ridge is accommodated in south Iceland, we compare surface velocities measured by GPS and corrected for coseismic offsets, with and without corrections for local volcanic deformation, to those predicted by a model of dike opening. The Eastern and Western volcanic zones are modeled as two parallel, infinitely long buried tensile cracks (dikes) in an elastic half-space. The dikes open continuously at some rate below some depth, above which they are locked (locking depth; appropriate for the interrifting period). There are three variables for each dike in this model: the locking depth, d, the dike-normal displacement, u, and the horizontal location of the spreading axis, x (Figure 10). Thus, for two parallel spreading ridges, up to six parameters may be estimated. The locking depth and dike location may be fixed using additional information (e.g., seismicity provides information on locking depth, and geologic observations may constrain dike location). Since the model is linear-elastic, deformation from adjacent rifts (EVZ and WVZ) can be calculated separately and summed. We use the formulation of *Okada* [1985] to calculate the corresponding surface velocity field. We perform a forward model (grid search) to estimate optimum parameter values, determining the minimum misfit between data and model as defined by the χ^2 function, which weights misfit by the square of the measurement error:

$$\chi^2 = \sum_{i=1}^{N} \frac{(O_i - C_i)^2}{\sigma_i^2} \tag{1}$$

Here O_i is a velocity or rate observation, C_i is the calculated (model) velocity or rate at the same location, σ_i is the measurement uncertainty, and N is the number of data. The minimum χ^2 indicates the best fit model. Since our error model accounts for the major factors that impact GPS site velocity uncertainty, we believe that the weighting and corresponding parameter estimation is robust. In its normalized form, χ^2_ν, (1) is divided by the number of degrees of freedom, $N - \nu$, where ν is the number of adjustable parameters. Both formulations are listed in Table 9.

[23] Parameter uncertainties are estimated using the F distribution to estimate the χ^2 misfit value corresponding to the appropriate confidence interval, e.g., 95%:

$$\chi^2_{95\%} = \chi^2_{\text{best}} \left[1 + \left(\frac{\nu_1}{\nu_2 - \nu_1} \right) F \right] \tag{2}$$

where χ^2_{best} is the best fit χ^2 value, ν is the number of adjusted parameters (generally 4 or 6), N is the number of data (11–32), and F is computed at $F_{\nu,N}$. Ancillary data are used to constrain the search area for the estimated parameters, as described below.

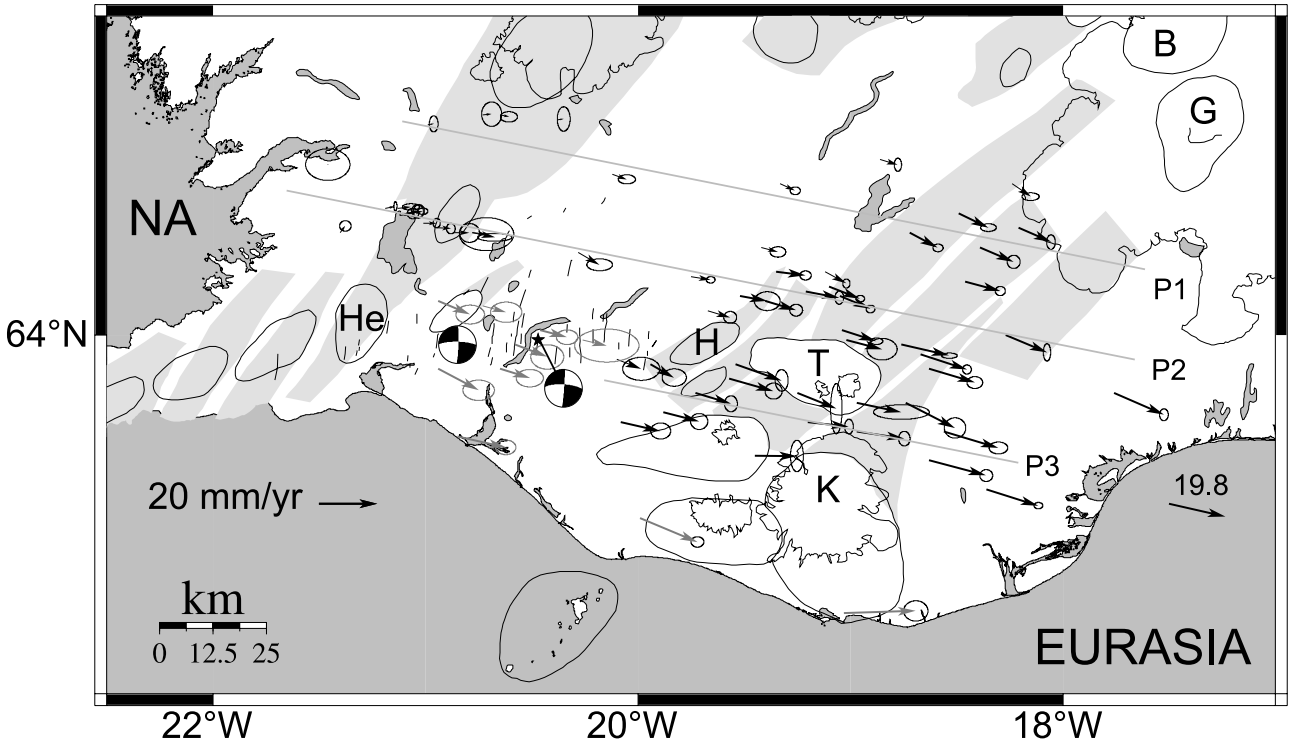

Figure 8. GPS velocity field relative to stable North America corrected for coseismic offsets from the 17 and 21 June 2000 SISZ earthquakes. Symbols are as in Figure 4 except gray arrows, which are pre-2000 velocities for sites located in the South Iceland Seismic Zone and are not used in the modeling. See Figure 5 for coseismic displacements. The locations of the profiles modeled in this study are shown (light grey lines).

[24] In elastic half-space models of strike-slip faults, the locking depth is often equated to the seismogenic thickness of the crust [*Savage and Burford*, 1973]. We make the same assumption for our model of lithospheric extension. Earthquake relocations in the SISZ show an eastward increase in seismogenic depth from 6 to 12 km [*Stefánsson et al.*, 1993]. Seismic reflection and gravity data suggest a large range of upper crust thickness in south Iceland, from 0.7–11 km, and also suggest a thinner elastic crust for the WVZ [*Darbyshire et al.*, 2000; *Du and Foulger*, 2001; *Foulger et al.*, 2003]. We initially fixed locking depths to 7.5 km (WVZ) and 10 km (EVZ), then investigated more complex models, treating locking depth as an adjustable parameter with a range from 0 to 15 km in both zones.

[25] The location and areal extent of the neovolcanic zones is constrained by geologic studies and historical rifting events (Figures 2 and 3) [*Jóhannesson et al.*, 1990]. Visual inspection of the velocity field (above) gives an indication of the location of the maximum velocity gradient within each neovolcanic zone. However, we treated the location of the maximum velocity gradient (central axis) as an adjustable parameter with a search area corresponding to the mapped extent of Holocene magmatic and tectonic activity.

[26] The total spreading rate for the Mid-Atlantic Ridge at the latitude of Iceland is known from both the NUVEL-1A (~3 Myr average) and REVEL (about decadal average) plate motion models [*DeMets et al.*, 1994; *Sella et al.*, 2002]. In the vicinity of Iceland, the total spreading rate is ~18–20 mm/yr in either model (Figure 1). We solve for the amount of dike-normal opening, u, for both extensional zones, and corresponding spreading rate, r, across each ridge segment during the period of our measurements. We search a range of dike-normal opening rates between 0 and 24 mm/yr for both neovolcanic zones, but do not constrain the total spreading rate to any value. Hence the summed rates estimated in our models serve as an independent check on results, assuming no significant deformation is occurring outside the two neovolcanic zones.

7.1. Volcanic Deformation

[27] Profile 1 is sufficiently far from volcanic centers active during the observation period that we can ignore the effects of local volcanic deformation on these site velocities. However, profiles 2 and 3 are affected by volcanic deformation. For profile 2, we present four sets of models based on 4 data subsets (Table 9). First, all sites were left uncorrected for Hekla deformation (model P2-3a). Second, sites most affected (i.e., three sites along the EDM line, D350, D353 and D356, and all sites within 24 km of Hekla) were removed from the profile (model P2-3b). Third, sites were corrected for Hekla deformation as described above (model P2-3c). Fourth, data were corrected for both Hekla and Hengill deformation (model P2-3d). For profile 3, site EINH is the only site affected by volcanic deformation at Eyjafjallajökull; we remove it from the profile, and correct remaining site velocities for the effects of Hekla and Katla deformation (model P3-1; Tables 4 and 6).

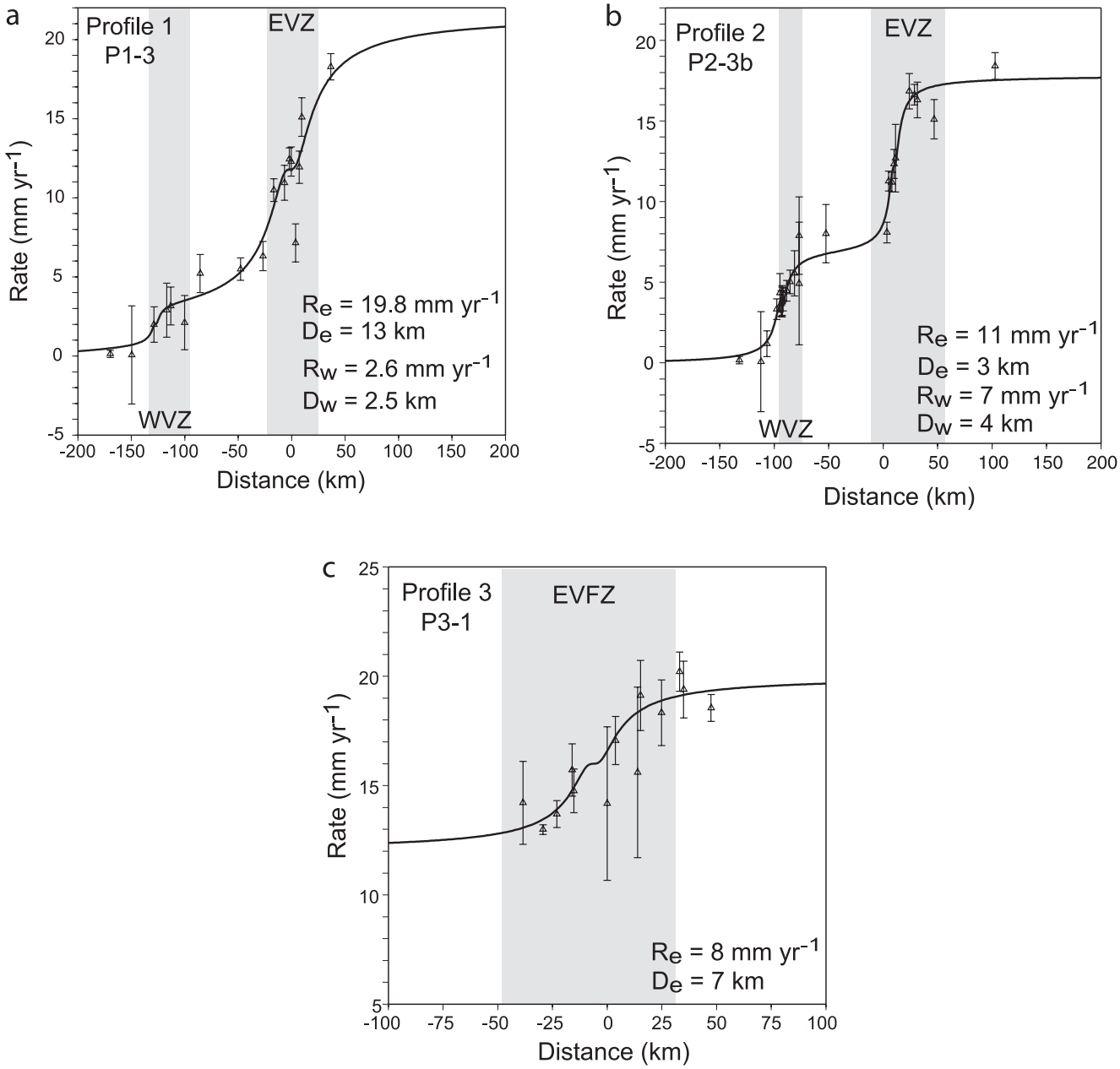

Figure 9. (a) GPS-derived site velocities relative to stable North America for sites within 10 km of profile 1. Rate component parallel to the plate motion direction (N102°E) is plotted. Error bars are 1-sigma uncertainties for the longitudinal component. Black line is best fit elastic half-space model (P1-3). Best fit model parameters are given: rate east (R_e), rate west (R_w), depth east (D_e), and depth west (D_w). Gray area denotes the Holocene location of Eastern and Western volcanic zones. (b) GPS-derived site velocities relative to stable North America for sites within 10 km of profile 2 and best fit elastic half-space model (P2-3b). Symbols are the same as in Figure 9a. (c) GPS derived site velocities relative to stable North America for sites within 10 km of profile 3 and best fit elastic half-space model (P3-1). Symbols are the same as in Figure 9a.

[28] Model parameter estimates and uncertainties are summarized in Table 9. Two suites of models were run for profiles 1 and 2. First, only the horizontal locations (x_e and x_w) and spreading rates (r_e and r_w) of the volcanic zones were estimated (four adjustable parameters), while the locking depth for both the EVZ and WVZ were fixed. Second, the horizontal locations, spreading rates and locking depths (six adjustable parameters) were estimated. In general, misfit is reduced with more adjustable parameters. The F test (e.g., *Stein and Gordon* [1984]) suggests that depth estimation is warranted in most cases. Results of the six-parameter models are used in the remaining discussion. Figures 11 and 12 display contoured values of misfit for pairs of estimated parameters, including the 95% confidence region, for models P1-3 and P2-3b, respectively.

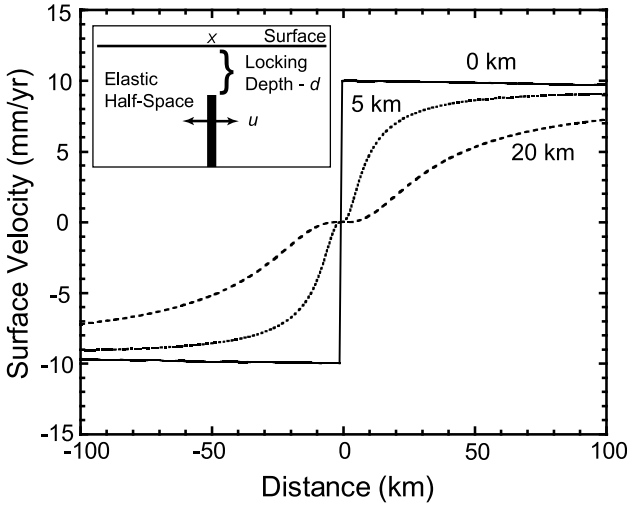

Figure 10. Diagram of the elastic half-space model used here to investigate the secular spreading signal across the overlapping spreading centers in South Iceland. Parameters (inset) are discussed in the text. The tensile crack or dike modeled here is infinite and represents continuous opening at depth. Predicted surface velocities for a single dike, shown for various locking depths: 20, 5, and 0 km (breaching the surface).

7.2. Model Results

7.2.1. Profile 1

[29] Spreading rates for the WVZ (2.6 ± 0.9 mm/yr) and EVZ (19.8 ± 2.0 mm/yr) are well constrained, giving a total spreading rate of 22.4 ± 2.2 mm/yr. The locking depths along this profile are not well constrained. While the EVZ locking depth (13.0 + 6.0/−3.0 km) is consistent with independent estimates for elastic thickness [*Foulger et al.*, 2003; *Stefánsson et al.*, 1993], the depth estimate for the WVZ (2.5 km) appears to be anomalously shallow and is essentially unconstrained (Figure 11). The models predict that the axis of spreading in the EVZ is located east of the Bárðabunga-Veidivötn fissure swarm (Figures 3 and 9a), consistent with visual inspection of the velocity profile. The axis of spreading in the WVZ is located at the neovolcanic zone's western edge, east of site UXAV (Figures 2 and 9a). The large uncertainties for locking depth and location of maximum velocity gradients in the WVZ reflect sparse data coverage (only four sites) (Figure 11).

7.2.2. Profile 2

[30] Spreading rate and locking depth estimates are similar for all profile 2 models, with results overlapping within uncertainties at the 95% confidence level (Table 9). The results of model P2-3b, our lowest misfit model, are used in the remaining discussion (site velocities corrected for coseismic offsets; sites most affected by Hekla deformation removed from the profile; no other corrections). The spreading rates for the WVZ (7.0 ± 0.4 mm/yr) and EVZ (11.0 ± 0.8 mm/yr) are well constrained (Figure 12), with a total spreading rate of 18.0 ± 0.9 mm/yr. The locking depths for the WVZ (4.0 + 2.1/−1.1 km) and EVZ (3.0 + 1.2/−0.7 km) are also well constrained and equivalent within uncertainties (Figure 12). Our results are somewhat shallower than independent seismic estimates. For example, *Darbyshire et al.* [2000] note that the average upper crustal thickness across Iceland is 5 km. *Foulger et al.* [2003] note a range of estimates (0.7–11 km) and prefer an average of 7 ± 1 km. Our models predict that the axis of spreading in the EVZ is located on the eastern edge of the Bárðabunga-Veidivötn fissure swarm (Figures 3 and 9b); this location is well constrained, consistent with the visual inspection of the velocity profile, consistent with profile 1 and west of Lakagígar. The axis of spreading in the WVZ is located on the Almannagja fissure at the western boundary of the Thingvellir Graben (Figures 2 and 9b).

7.2.3. Profile 3

[31] Profile 3 (Eastern Volcanic Flank Zone) has a spreading rate of 8.0 ± 1.0 mm/yr and locking depth of 7.0 + 2.5/−1.5 km (Table 9). The axis of spreading is located south of Torfajökull on a Holocene fissure aligned with the Bárðabunga-Veidivötn fissure to the north (Figures 3 and 9c).

8. Viscoelastic Modeling and Rifting Cycle Effects

[32] The elastic half-space models described in section 7 fit the geodetic data quite well. Nevertheless, the elastic half-space model is an oversimplification in terms of crustal and upper mantle rheology and does not allow for investigation of rifting cycle effects. Purely elastic models may give biased rate estimates, especially for pairs of adjacent faults in different parts of the earthquake cycle [*Dixon et al.*,

Table 9. Elastic Half-space Model Parameter Estimates and Uncertainties[a]

Model	Number of Data	Number of Adjustable Parameters	Rate EVZ, mm/yr	Rate WVZ, mm/yr	Total Rate, mm/yr	Depth EVZ, km	Depth WVZ, km	χ^2	χ_ν^2
P1-1	17	4	17.2 ± 1.5	4.0 ± 0.8	21.2 ± 1.7	(10)	(7.5)	29.30	2.44
P1-3	17	6	19.8 ± 2.0	2.6 ± 0.9	22.4 ± 2.2	13.0 + 7.0/−3.3	2.5[b]	27.20	2.72
P2-1a	32	4	14.0 ± 1.0	5.0 ± 0.5	19.0 ± 1.1	(10)	(7.5)	74.31	2.64
P2-3a	32	6	11.2 ± 1.0	7.4 ± 0.5	18.6 ± 1.1	4.5 + 2.0/−1.0	4.0 + 3.0/−1.2	45.78	1.76
P2-1b	25	4	14.6 ± 1.3	6.2 ± 0.6	20.8 ± 1.4	(10)	(7.5)	59.89	2.85
P2-3b	25	6	11.0 ± 0.8	7.0 ± 0.4	18.0 ± 0.9	3.0 + 1.2/−0.7	4.0 + 2.1/−1.1	17.26	0.90
P2-1c	32	4	13.0 ± 1.0	5.6 ± 0.5	18.6 ± 1.1	(10)	(7.5)	68.93	2.46
P2-3c	32	6	12.2 ± 1.0	5.8 ± 0.5	18.0 ± 1.1	7.5 + 2.7/−1.7	3.0 + 3.6/−1.1	51.24	1.97
P2-1d	32	4	14.0 ± 1.3	7.0 ± 0.5	21.0 ± 1.4	(10)	(7.5)	67.02	2.39
P2-3d	32	6	9.6 ± 0.8	8.4 ± 0.4	18.0 ± 0.9	2.5 + 1.3/−0.8	5.0 + 2.5/−1.3	30.31	1.16
P3-1	11	3	8 ± 1.0	-	-	7.0 + 2.5/−1.2	-	4.70	0.47

[a]Uncertainties are one standard error; χ^2 is the misfit of data versus model weighted by the measurement error. Values in parentheses were held fixed in the models.

[b]This depth estimate can not be constrained within reasonable values of crustal thickness.

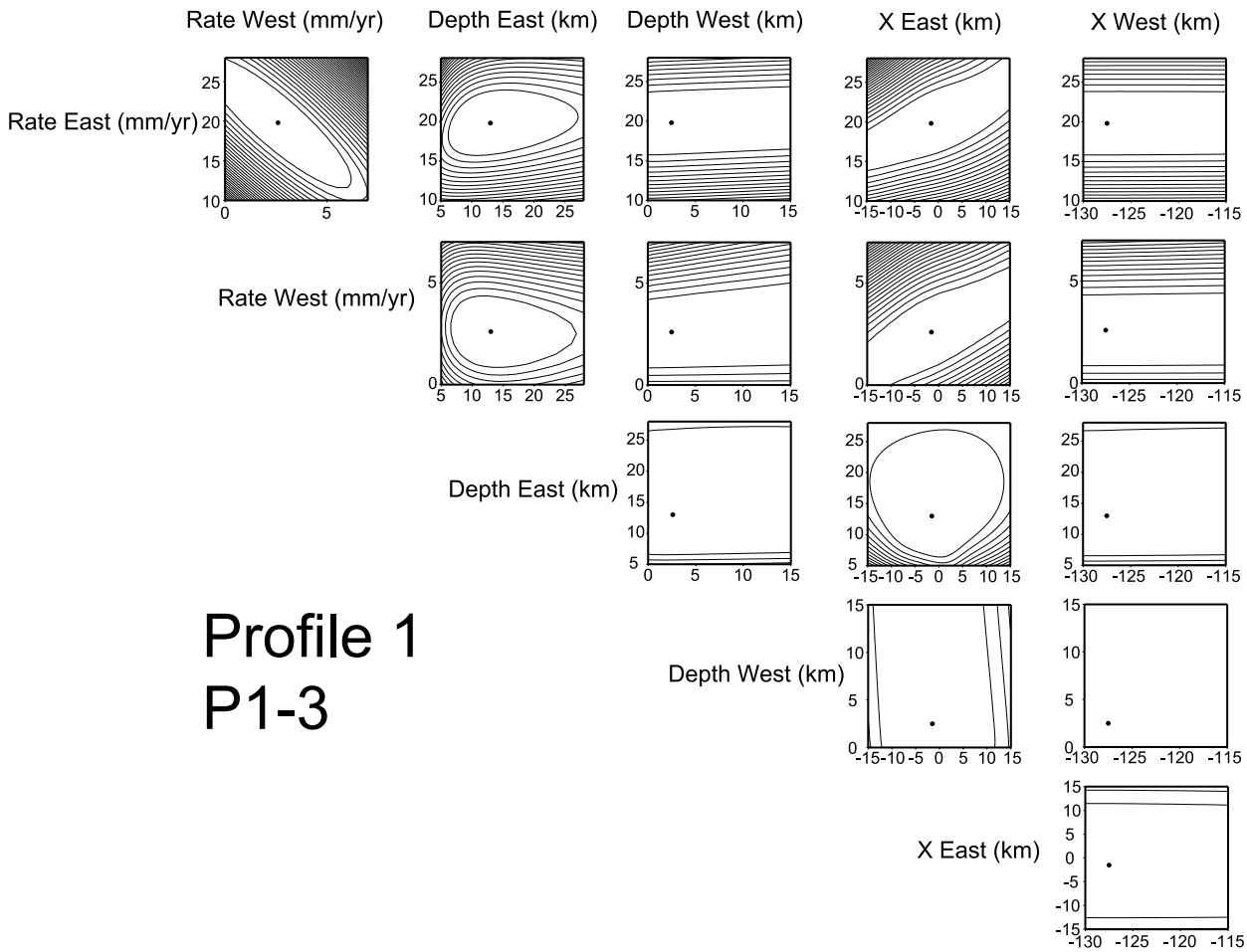

Figure 11. Contour plots of χ^2 misfit for pairs of estimated parameters for elastic half-space model P1-3 (profile 1). Four parameters were held at best fit values to calculate misfit for the other two parameters; χ^2 equal to 72 (inner contour) represents approximate 95% confidence limit. Contour interval is 20.

2002, 2003] or for faults late in the earthquake cycle [*Malservisi et al.*, 2003]. In particular, for two or more adjacent faults, the total rate accommodated across the deforming region is generally well constrained by GPS and is insensitive to choice of rheological model, but partitioning of strain and estimation of individual fault slip rates may be highly model-dependent. Similar biases might affect our spreading rate estimates. One of our goals is to assess partitioning between the EVZ and WVZ, requiring us to explore the possible dependence of our results on choice of rheological model.

[33] Models incorporating an elastic layer over one or more viscoelastic layers are probably more realistic, have been developed for Iceland [*Hofton and Foulger*, 1996; *Pollitz and Sacks*, 1996], and, since we know the dates of major rifting events, can account for rifting cycle effects. To investigate possible effects of the rifting cycle on our spreading rate and locking depth estimates, we use a simple coupling model with an upper elastic layer coupled to an underlying Maxwell (linear) viscoelastic half-space (Figure 13). The viscoelastic properties of the half-space generate time-varying deformation associated with periodic rifting events. The coupling model is implemented with a finite element technique, using the publicly available code TECTON [*Govers*, 1993; *Melosh and Raefsky*, 1981] in a two-dimensional formulation, analogous to the elastic half-space model described in section 7. The model does not account for gravitational or isostatic forces, therefore the surface has a no vertical displacement boundary condition. The viscoelastic half-space is simulated with a large model space (500 km depth, 1000 km lateral dimension) and is laterally homogeneous in thickness and rheology. For both elastic and viscoelastic materials, Poisson's ratio is 0.25 and Young's Modulus is 75 GPa. To test our coupling model, we initially set half-space viscosity to high values, obtaining results essentially identical to the analytical elastic half-space results described in section 7.

[34] We fixed the location and extension rates of the neovolcanic zones based on results of the elastic half-space models, and investigated the influence of the rifting cycle (time since last rifting event), half-space viscosity, and elastic layer thickness along profile 2 (model P2-3b). The model assumes strictly periodic rifting events, with the recurrence interval based on geologic or historical data. Boundary conditions for the model are shown in Figure 13. The western boundary is held fixed and the eastern boundary given a horizontal velocity equal to the total geodetic spreading rate, 18 mm/yr. These boundary conditions are analogous to a fixed North American reference frame.

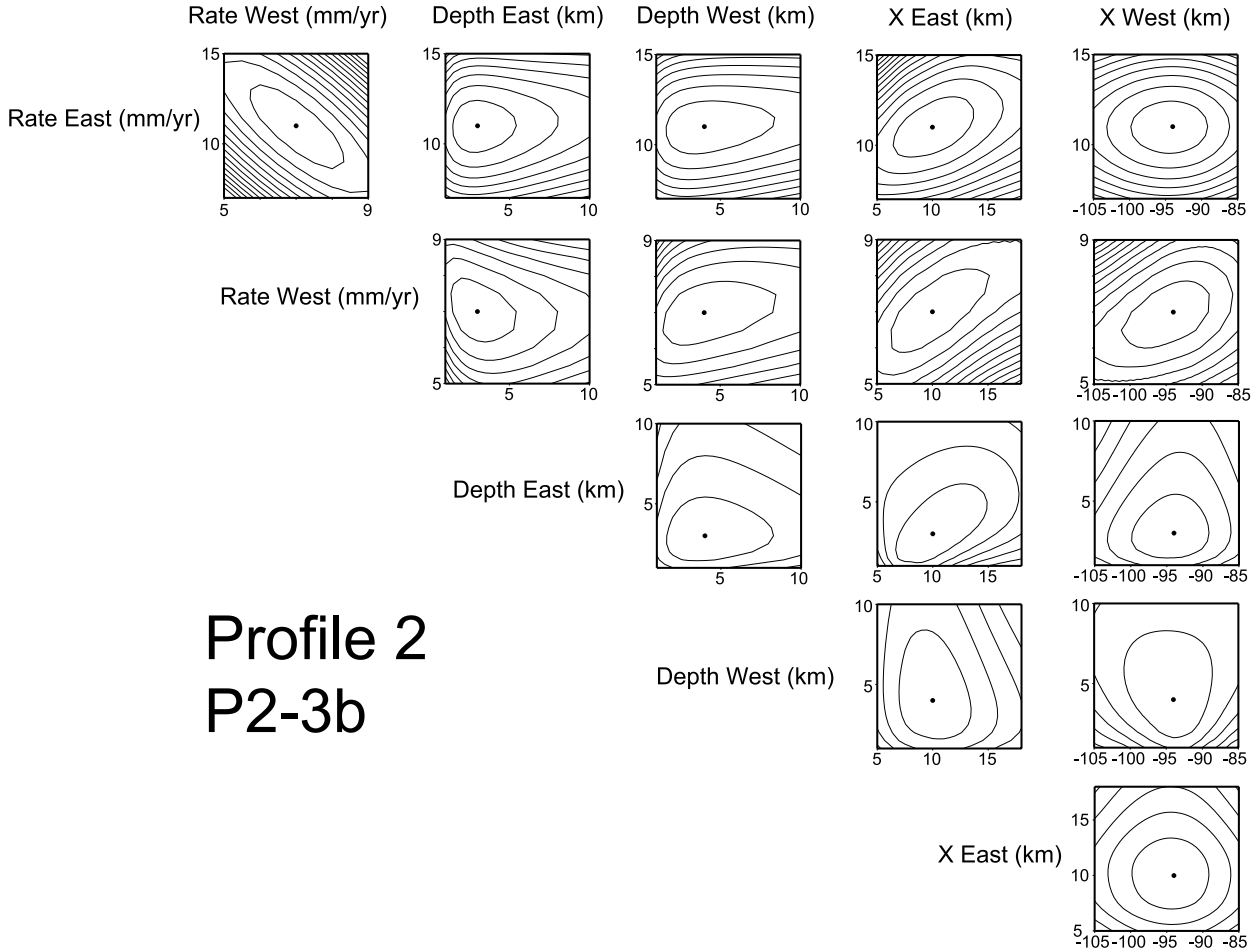

Figure 12. Similar to Figure 11 but for model P2-3b (profile 2). Here χ^2 equal to 31 (inner contour) represents 95% confidence limit. Contour interval is 20.

[35] Previous viscosity estimates for the lower crust and upper mantle beneath Iceland have been based on geologic and geodetic studies of postglacial rebound, and of postdiking and postseismic stress relaxation. *Sigmundsson* [1991] and *Sigmundsson and Einarsson* [1992] investigated historical retreat of Vatnajökull ice cap and estimated viscosities in the range 10^{18} to 10^{19} Pa s for the lower crust and upper mantle. The 1975–84 Krafla rifting event enabled study of postdiking stress relaxation. *Hofton and Foulger* [1996] used GPS data and a model with an elastic-gravitational layer overlying a viscoelastic-gravitational half-space to estimate a half-space viscosity of 1.1×10^{18} Pa s. *Pollitz and Sacks* [1996] modeled the same data set, but used a multilayered earth model, obtaining viscosities for the lower crust and upper mantle of 3×10^{19} and 3×10^{18} Pa s, respectively. We tested half-space viscosities between 10^{18} and 10^{20} Pa s.

[36] We simulate rifting events by opening a vertical dike through the entire elastic layer by amounts and with recurrence times such that the quotient equals the estimated spreading rates from the elastic half-space models. In this way the dike acts to periodically relax the stress within the elastic layer associated with the displacement boundary condition. The mean recurrence time for historical rifting events in the EVZ is ~250 years (Table 1). Using model P2-3b (Table 9), a total displacement of ~2.75 m is required to obtain the ~11 mm/yr spreading rate. The mean recurrence time for the four documented rifting events in the WVZ is ~500 years [*Sæmundsson*, 1992]; a total displacement or dike thickness of ~3.5 m per rifting event is then required to obtain the ~7 mm/yr spreading rate. The actual amount of extension may vary during each rifting event. For example, extension in the last WVZ rifting event (1789) was 1.0–2.6 m [*Sæmundsson*, 1992]. Estimated dike openings for the EVZ exhibit similar variability (Table 1).

[37] The models were run until the surface velocity reached steady state (i.e., the difference between two consecutive rifting cycles was negligible) typically 14–20 rifting cycles, depending on half-space viscosity. We inspect the surface velocity field at time intervals related to the last known rifting events for the WVZ and EVZ, approximately 200 and 150 years, respectively. Figure 14 compares results for the elastic half-space model and the best fit viscoelastic model for an elastic layer thickness of 3 km. The viscoelastic coupling models fit the data about as well as the elastic model for the same spreading rates. We conclude that our rate and depth estimates are not biased by our choice of rheological model. These results are perhaps not surprising, since both rift zones are at a similar stage (middle) of their respective rifting cycle based on geologic data, and large postrifting strain transients have presumably decayed. We

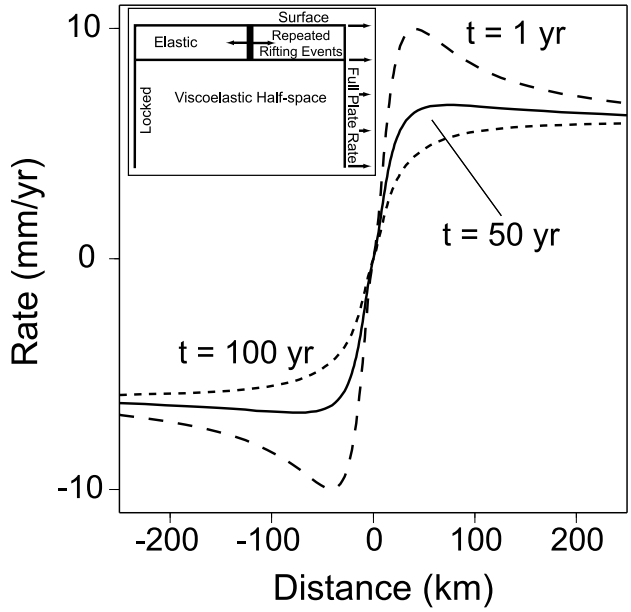

Figure 13. Predicted surface velocities for a single dike, 1, 5, and 100 years after a rifting event, for a viscoelastic coupling model. Inset is a diagram of model (parameters discussed in text). The dike cuts the entire elastic layer and opens periodically for each spreading center at recurrence intervals based on historical fissure eruptions.

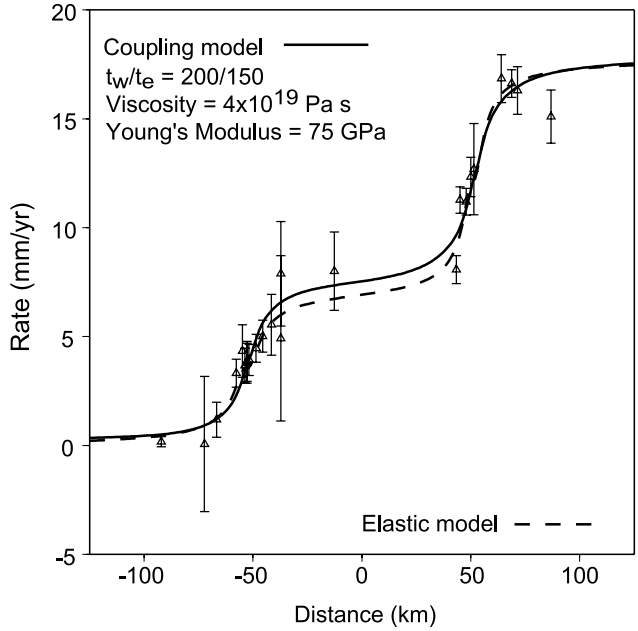

Figure 14. Best fit coupling model compared to GPS-derived site velocities relative to stable North America for profile 2. The modeled velocity field is 200 and 150 years after the last rifting event on the WVZ (t_w) and EVZ (t_e), respectively. Error bars are the 1-sigma rate uncertainties for the longitudinal component. Dashed line is best fit elastic half-space model from Figure 9b.

conclude that the elastic half-space model is adequate for this application, and does not yield biased results.

[38] The coupling model does provide some additional information, in this case an independent estimate of average viscosity beneath the elastic crust. Figure 15 plots model misfit as a function of viscosity and elastic layer thickness. While there is some trade-off between these two parameters, for a reasonable range of elastic layer thickness, half-space viscosity is in the range 2×10^{19} to 1×10^{20} Pa s. We did not investigate possible trade-offs with other model parameters, e.g., the amount of dike opening per rift event, which could also influence results.

9. Hreppar Block

[39] Our surface velocity data are well fit by a simple model of dike injection and deformation on the EVZ and WVZ, with no permanent deformation in the intervening region, the Hreppar block. This suggests that the velocity data in the Hreppar block fit a rigid microplate or block model, with the block deforming only by elastic strain accumulation on its edges. By choosing sites in the interior of the block, we may be able to avoid most of this elastic deformation and define motion of the Hreppar block in terms of rigid block rotations on a sphere, analogous to the motions of larger plates, with a simple inversion for the block's angular velocity.

[40] Figure 16 shows site velocities for south Iceland relative to the Hreppar block. The coseismic corrected velocities are used here. The five sites used to define the Hreppar block fit the rigid block model to better than 1 mm/yr. Studies of propagating ridges and overlapping spreading centers predict that the overlap region (e.g., the Hreppar

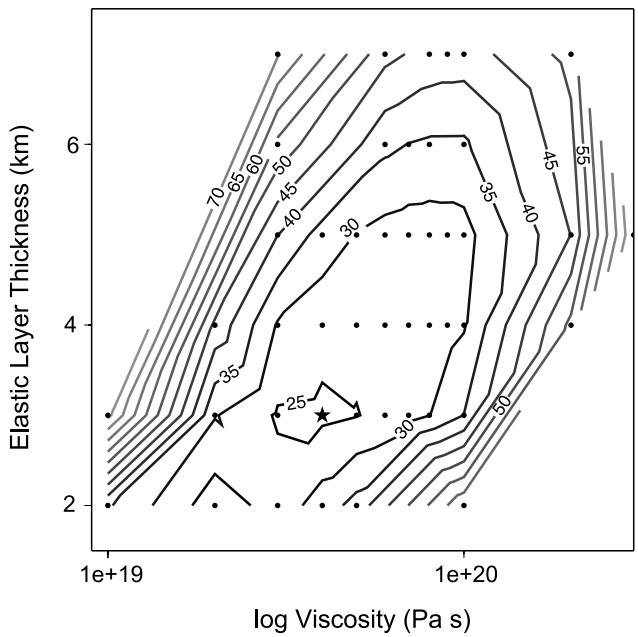

Figure 15. Contour plot of χ^2 misfit for viscosity versus elastic layer thickness for viscoelastic coupling models. Black dots show tested values. Contour interval is 5; χ^2 equal to 30 represents approximate 95% confidence limit. Star denotes best fit model (4×10^{19} Pa s and 3 km).

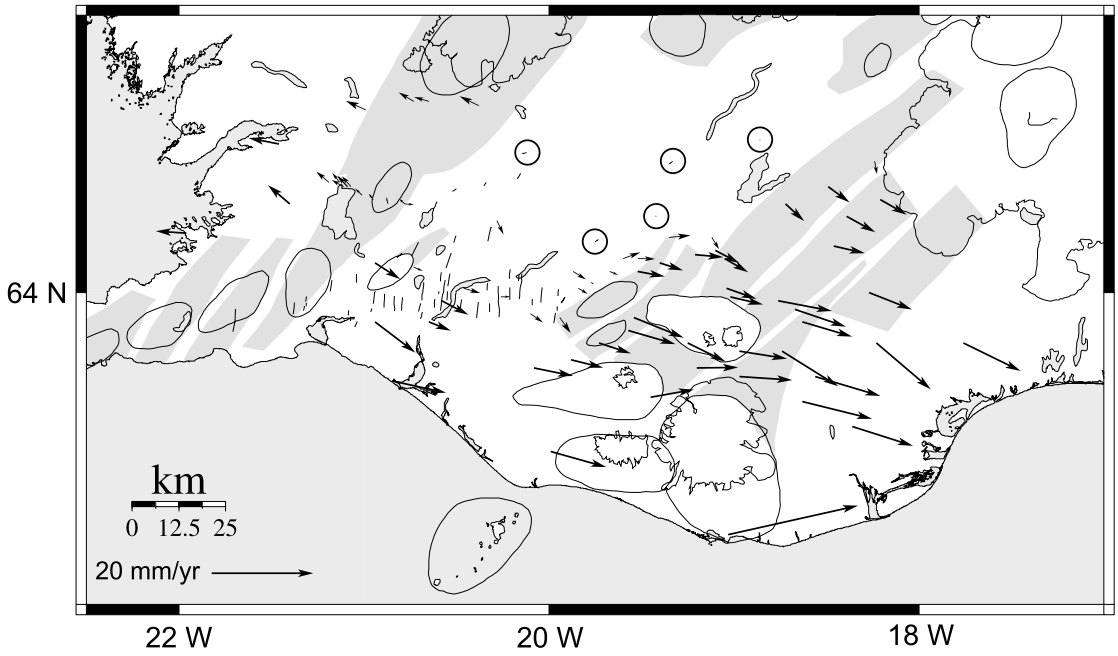

Figure 16. GPS velocity field relative to the Hreppar block, corrected for coseismic offsets from the 17 and 21 June 2000 SISZ earthquakes. Five sites used to define the Hreppar block are circled. This velocity field shows the slower divergence across the WVZ relative to the EVZ and strain accumulation across the SISZ. Deformation at sites near Hekla volcano can also be seen.

Block) will act either as a rigid block or deform internally via shear [*Engeln et al.*, 1988]. Our data suggest that the Hreppar Block in fact is rigid, at least to the level of our data uncertainty.

10. Discussion

[41] The Mid-Atlantic Ridge at the latitude of Iceland is an unstable plate boundary. West-northwest motion of the plate boundary relative to the Iceland hot spot has caused repeated east-southeast jumps of the neovolcanic zone since ~23 Ma [*Garcia et al.*, 2003; *Hardarson et al.*, 1997; *Oskarsson et al.*, 1985], the latest of which occurred at ~2–3 Ma in south Iceland forming the EVZ. Ridge jumps in south Iceland result in overlapping spreading centers, with the eastern limb propagating and western limb deactivating toward the southwest. Geologic and geochronologic studies in northern and western Iceland demonstrate the evolution of the neovolcanic zones over millions of years [*Garcia et al.*, 2003; *Hardarson et al.*, 1997]. These studies indicate rise and deactivation times on the order of 6–8 Myr, with individual rift activity lasting up to 12 Myr, but lack the spatial sampling to investigate the kinematic effects of propagating ridges and overlapping spreading centers. Our observations have implications for strain accumulation and partitioning, and the mechanics of crustal accretion in a propagating ridge system.

10.1. Along-Strike Variability in Spreading Rates

[42] In a propagating ridge system, strain (extension) will be partitioned between overlapping spreading centers, with the sum of spreading across both centers totaling the full plate rate [*Hey*, 1977; *Hey et al.*, 1980]. The amount of extension will increase on the deactivating limb and decrease on the propagator, in the direction of propagation. Therefore the ratio of spreading rates between the neovolcanic zones in Iceland should be latitude-dependent. Our spreading rate estimates for profiles 1 and 2 (the two profiles that cross both active rift zones) indicate along-strike variations across the EVZ and WVZ, with summed rates consistent with independent estimates of total North America–Eurasia plate motion (Table 10 and Figure 17). This suggests that the EVZ and WVZ together accommodate essentially all of North America–Eurasia plate motion. Our estimate for spreading rate across the Eastern Volcanic Flank Zone (EVFZ) (i.e., profile 3; 8 mm/yr), south of the SISZ in the actively propagating section, suggests that an additional ~11 mm/yr of motion is accommodated across the Reykjanes Peninsula [e.g., *Hreinsdóttir et al.*, 2001]. Results for profile 2 are in agreement with previous geodetic estimates, within uncertainties [*Jónsson et al.*, 1997; *Sigmundsson et al.*, 1995; *Tryggvason*, 1982].

[43] Figure 17 schematically shows the results of the elastic half-space models and illustrates the partitioning of spreading rates across the Mid-Atlantic Ridge in south Iceland. The spreading rates increase north to south in the WVZ, from 2.6 to 7.0 mm/yr, respectively. Conversely, the rates decrease north to south in the EVZ and into the EVFZ,

Table 10. Spreading Rate Estimates From the Elastic Half-Space Models Compared With the REVEL 2000 and NUVEL-1a Plate Motion Models[a]

Profile	WVZ	EVZ	Total	REVEL	NUVEL-1A
1	2.6 ± 0.9	19.8 ± 2.0	22.4 ± 2.2	19.7	18.4
2	7.0 ± 0.4	11.0 ± 0.8	18.0 ± 0.9	19.8	18.4
3	?	8.0 ± 1.0	?	19.9	18.5

[a]See *DeMets et al.* [1994] and *Sella et al.* [2002].

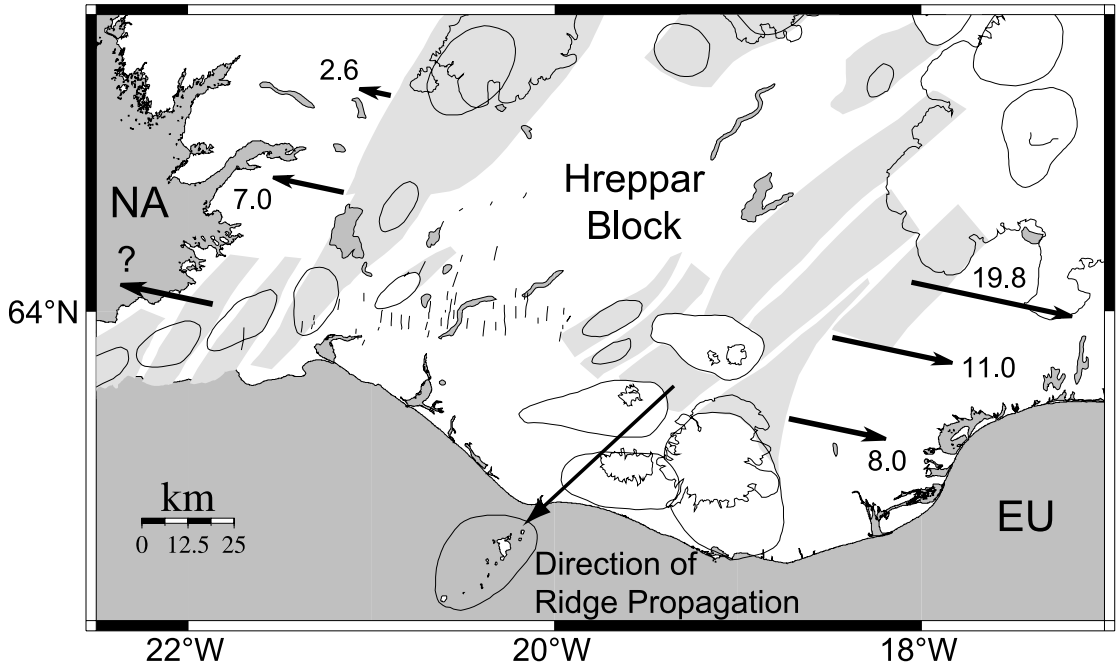

Figure 17. Map of spreading rates estimated with our elastic half-space models for profiles 1, 2, and 3. The along-strike variations in spreading rate match a propagating ridge model, where the WVZ is deactivating and EVZ is activating toward the southwest, the direction of ridge propagation.

from 19.8 to 11.0 and to 8 mm/yr, respectively. This pattern is consistent with a simple propagating ridge model, with the EVZ propagating and WVZ deactivating to the southwest. Thus it is not possible to determine a single ratio that describes relative spreading rates across the two volcanic zones; the ratio is latitude-dependent.

10.2. Crustal Accretion

[44] The new GPS data provide some additional insights into the crustal accretion process. For example, it has generally been assumed that development of overlapping spreading centers and intervening micro plate is restricted to fast spreading ridges, since they are mainly described for the East Pacific Rise [e.g., *MacDonald and Fox*, 1983]. However, the Hreppar block and its bounding neovolcanic zones manifest most characteristics of a standard overlapping spreading center–microplate model. Presumably the proximal location of the Icelandic hot spot promotes development of the overlapping spreading center system through repeated ridge jumps and ridge propagation.

[45] Geologic studies in Iceland and relic segments of mid-ocean ridges (e.g., Oman ophiolite) indicate that plate motion is accommodated by repeated injection of dikes into the crust [*Bodvarsson and Walker*, 1964; *Gudmundsson*, 2000; *Sigurdsson and Sparks*, 1978; *Walker*, 1960]. This process results in formation of new oceanic crust and controls ridge morphology. For example, the fast spreading East Pacific Rise has high rates of volcanism and low topographic relief, whereas the slow spreading Mid-Atlantic Ridge has lower rates of volcanism and a pronounced axial graben.

[46] The geomorphology of the neovolcanic zones in south Iceland reflects their differences in spreading rate and magma supply. The northern end of the EVZ, marked by the central volcanoes Bárðarbunga and Grimsvötn, is the proposed location of the Iceland hot spot [*Bjarnason et al.*, 1993]. In this region there has been extensive postglacial volcanism and elevated topography with few graben structures. These features give the EVZ the appearance of a fast spreading ridge (e.g., the East Pacific Rise), even though the actual spreading rate is slow. In contrast, the slower spreading WVZ has had fewer postglacial eruptions, has a pronounced axial graben and may be magma starved. In fact, it may only be fed by north directed lateral magma injection from the Hengill central volcano [*Bull et al.*, 2003; *Gudmundsson*, 1987; *Sæmundsson*, 1992].

[47] The last major event in the EVZ was the 1783–1784 Lakagígar fissure eruption, and it might be expected that this would be the current locus of diking and strain accumulation. However, strain in the EVZ is currently centered on the eastern Bárðarbunga-Veidivötn fissure swarm, ~20 km to the west. Crustal accretion in the EVZ has historically occurred along these two discrete neovolcanic zones, each ~20 km wide and ~30 km apart (center to center). The Bárðarbunga-Veidivötn fissure last erupted in 1862–1864, during the small volume Trollagigar eruption, ~20 km north of profile 1 and ~50 km north of profile 2 (Table 1 and Figure 3). The last large volume eruption of Veidivötn occurred in 1477 [*Larsen*, 1984]. The location of our maximum velocity gradient is consistent with the results of *Decker et al.* [1971] and *Jónsson et al.* [1997]. They attributed this pattern of deformation (i.e., maximum velocity gradient across Bárðarbunga-Veidivötn fissure swarm) to eruptions of Hekla volcano, ~25 km south-southwest of profile 2. However, our profile 1 is far enough away from Hekla volcano to be unaffected by its deformation, indicating that this pattern is consistent along a longer segment of

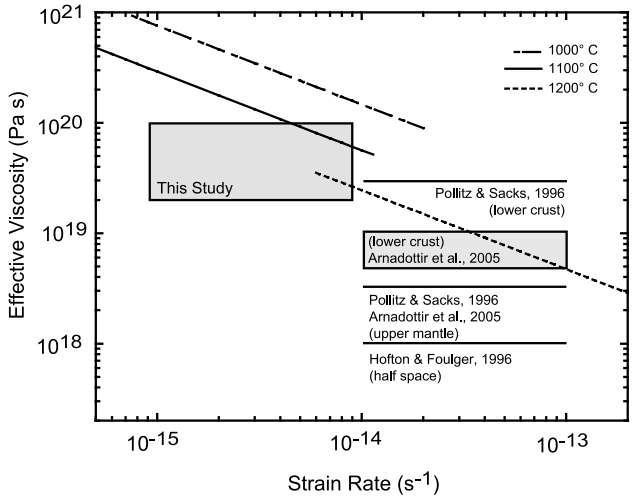

Figure 18. Viscosity versus strain rate estimates for Iceland based on modeling of crustal deformation as measured by geodetic GPS data for early postrifting stage [*Hofton and Foulger*, 1996; *Pollitz and Sacks*, 1996] assuming characteristic strain rates of order 10^{-13} to 10^{-14} s^{-1}, and mid-late rifting stage (this study) assuming strain rates of order 10^{-14} to 10^{-15} s^{-1}. Solid and dashed lines show 1000°C, 1100°C, and 1200°C estimates of effective viscosity for olivine from power law creep flow law calculated from equation 2 of *Dixon et al.* [2004].

the Bárðarbunga-Veidivötn fissure swarm and may be tectonic in origin.

[48] The spatial and temporal pattern of historical and documented eruptions suggests that rifting events (i.e., crustal accretion) in the EVZ jump from east to west and back (Table 1 and Figure 3). This pattern could reflect either stress interaction between fissure swarms, or variable supply of magma from central volcanoes to the fissure swarms, which may modulate the recurrence time and location of fissure eruptions.

10.3. Viscosity of South Iceland Upper Mantle

[49] Our viscosity estimate of $\sim 4 \times 10^{19}$ Pa s is higher than some previously published estimates for upper mantle viscosity based on geodetic data covering the high strain rate period following the Krafla rifting event of 1975–1984 [*Hofton and Foulger*, 1996; *Pollitz and Sacks*, 1996] (Figure 18). The viscosity estimate is sensitive to several aspects of the model parameterization, including the number and thickness of the various layers and their elastic properties. *Pollitz and Sacks* [1996] use an elastic upper crust over two viscoelastic regions representing the lower crust and upper mantle. We use a simplified model with an elastic layer over viscoelastic half-space; hence part of the difference may reflect the fact that our half-space represents an average between a stronger lower crust and weaker upper mantle. Also, the average Young's modulus could vary by up to a factor of 2o from our nominal value (75 GPa), resulting in a factor of 2 difference in the corresponding viscosity estimate. There is also a trade-off between viscosity and elastic layer thickness (Figure 15). However, even the thinnest plausible elastic layer results in a viscosity of 2×10^{19} Pa s, considerably higher than the upper mantle estimate of *Pollitz and Sacks* [1996], 3×10^{18} Pa s.

[50] Another possible factor is the influence of strain rate and temperature on effective viscosity. Our rheological model assumes a simple linear relation between stress and strain rate. However, laboratory results suggest that for moderately high stresses and strain rates, olivine, the major constituent of the upper mantle, deforms by power law (stress- and strain-rate-dependent) dislocation creep [*Brace and Kolhstedt*, 1980; *Hirth and Kolhstedt*, 2004; *Karato and Wu*, 1993; *Kirby*, 1983]. Power law behavior can nevertheless be approximated with linear viscoelastic models such as those used here by defining an effective viscosity at a given stress or strain rate [*Hirth and Kolhstedt*, 2004]. Despite the fact that laboratory conditions and actual fault or rift-related processes differ by many orders of magnitude in strain rate, comparison of the laboratory results to geodetic and geologic estimates of effective viscosity of the upper mantle in a number of regions and for a range of strain rates suggests that the approach is valid [*Dixon et al.*, 2004].

[51] Our velocity field reflects relatively low strain rate processes characteristic of the mid to late stage in the rifting cycle ($\sim 10^{14}$ to 10^{15} s^{-1}). Average temperature at a given depth in the lower crust may also be somewhat lower compared to the immediate postrifting period. Hence we expect to obtain higher effective viscosities compared to studies based on data acquired during higher strain rate ($\sim 10^{13}$ to 10^{14} s^{-1}) postrifting and postseismic periods. This is illustrated schematically in Figure 18, where we show the effect of strain rate and temperature on effective olivine viscosity, as well as several published viscosity estimates, assuming the broad strain rate categories listed above.

[52] In summary, our estimate of the average viscosity beneath the elastic upper crust is plausible. Though somewhat higher than other estimates based on early postrift deformation data, this could reflect at least in part the lower strain rates associated with the interrifting period. Until now, the rheology of this region, representing the lower crust and upper mantle, has been studied mainly from postglacial rebound or postseismic and postrifting geodetic data. Our work suggests that interrifting geodetic data can also provide useful constraints on the rheological properties of this region.

10.4. Implications of Shallow Locking Depth

[53] Our estimates of locking depth from both the elastic half-space and coupling models are relatively shallow. These depths should correspond approximately to the brittle-ductile transition depth for mafic material along the active rift axis. Since the temperature of this transition is known from laboratory measurements ($\sim$500°C), it is possible to use the GPS results to estimate the approximate geothermal gradient for the shallow crust at the rift axis. Assuming a locking depth of 3 km (coupling model result) gives a gradient of $\sim$165°C/km for upper crust within the neovolcanic zone. For comparison, geothermal drilling in the Reykjanes peninsula suggests upper crustal gradients of 100–160°C/km [*Flóvenz and Sæmundsson*, 1993; *Meyer et al.*, 1985]. Our depth estimates do not represent the

average elastic thickness of Icelandic crust, but rather the thickness in the immediate vicinity of the rift axis.

11. Conclusions

[54] 1. Along-strike variations in spreading rate in an overlapping spreading center system can be observed with geodetic GPS studies in Iceland and are consistent with a propagating ridge model for south Iceland, with the WVZ deactivating. The EVZ accommodates 55–100% of plate motion, depending on latitude.

[55] 2. The surface velocity data allow precise estimates of locking depth for a simple model of a continuously opening dike at depth below a locked upper crustal zone. The depths obtained for the EVZ are quite shallow (3–4 km), and correspond approximately to the maximum depth of earthquakes and the brittle-ductile transition depth at the rift axis.

[56] 3. The Hreppar block acts as a rigid block or microplate within the uncertainties of our velocity observations ($\sim$1 mm/yr), consistent with some overlapping spreading center models.

[57] 4. A simple coupling model (thin elastic layer representing the upper crust over a Maxwell viscoelastic half-space representing the lower crust and upper mantle) yields a viscosity estimate of $\sim 4 \times 10^{19}$ Pa s (range $2-10 \times 10^{19}$ Pa s).

[58] 5. Maximum strain accumulation in the EVZ occurs at the Bárðarbunga-Veidivötn fissure swarm, which last experienced a major eruption in 1470. Presumably this will be the site of the next major fissure eruption in the EVZ.

[59] **Acknowledgments.** The authors wish to thank all those who helped with the GPS observations, including Halldor Olafsson, Halldor Geirsson, Mattias Lindman, Thomas Walter, Heidi Soosalu, and the kind folks at Gunnarsholt. Discussions with Kevin Furlong and Rob Govers, and reviews by Fred Pollitz and Paul Tregoning, greatly improved the manuscript. Figures were made using GMT [*Wessel and Smith*, 1994]. This work was supported through NASA by a Florida Space Grant to P.L. and NASA, NSF, and ONR grants to T.H.D. The Icelandic Research Council, RANNIS, funded E.S.

References

Angelier, J., R. Slunga, F. Bergerat, R. Stefánsson, and C. Homberg (2004), Perturbation of stress and oceanic rift extension across transform faults shown by earthquake focal mechanisms in Iceland, *Earth Planet. Sci. Lett.*, *219*, 271–284.

Árnadóttir, T., S. Hreinsdóttir, G. Gundmundsson, P. Einarsson, M. Heinert, and C. Voelksen (2001), Crustal deformation measured by GPS in the South Iceland seismic zone due to two large earthquakes in June 2000, *Geophys. Res. Lett.*, *28*, 4031–4033.

Árnadóttir, T., S. Jónsson, F. Pollitz, W. Jiang, and K. L. Feigl (2003), Spatio-temporal variations of post-seismic deformation after the June 2000 earthquake sequence in southwest Iceland, *Eos Trans. AGU*, *84*(46), Fall Meet. Suppl., Abstract G21B-0268.

Árnadóttir, T., F. Pollitz, S. Jónsson, K. L. Feigl, E. Sturkell, H. Geirsson, and P. Einarsson (2005), Postseismic deformation following the June 2000 earthquake sequence in the south Iceland seismic zone, *J. Geophys. Res.*, doi:10.1029/2005JB003701, in press.

Bjarnason, I. T., W. Menke, O. G. Flovenz, and D. Caress (1993), Tomographic image of the Mid-Atlantic plate boundary in south-western Iceland, *J. Geophys. Res.*, *98*, 6607–6622.

Bodvarsson, R., and G. P. L. Walker (1964), Crustal drift in Iceland, *Geophys. J. R. Astron. Soc.*, *8*, 285–300.

Boucher, C., Z. Altamimi, and P. Sillard (1999), The 1997 International Terrestrial Reference Frame (ITRF-97), Obs. de Paris, Paris.

Brace, W. F., and D. C. Kolhstedt (1980), Limits on lithosphere stress imposed by laboratory experiments, *J. Geophys. Res.*, *85*, 6248–6252.

Brander, J. L., R. G. Mason, and R. W. Calvert (1976), Precise distance measurements in Iceland, *Tectonophysics*, *31*, 193–206.

Bull, J. M., T. A. Minshull, N. C. Mitchell, K. Thors, J. K. Dix, and A. I. Best (2003), Fault and magmatic interaction within Iceland's western rift over the last 9 kyr, *Geophys. J. Int.*, *154*, F1–F7.

Darbyshire, F. A., R. S. White, and K. F. Priestley (2000), Structure of the crust and uppermost mantle of Iceland from a combined seismic and gravity study, *Earth Planet. Sci. Lett.*, *181*, 409–428.

Decker, R. W., P. Einarsson, and P. A. Mohr (1971), Rifting in Iceland; new geodetic data, *Science*, *173*, 530–533.

Decker, R. W., P. Einarsson, and R. Plumb (1976), Rifting in Iceland: Measuring horizontal movements, *Science*, 67–71.

DeMets, C., R. G. Gordon, D. F. Argus, and S. Stein (1994), Effect of recent revisions to the geomagnetic reversal time scale on estimates of current plate motions, *Geophys. Res. Lett.*, *21*, 2191–2194.

Dixon, J. E., T. H. Dixon, D. R. Bell, and R. Malservisi (2004), Lateral variation in upper mantle viscosity: Role of water, *Earth Planet. Sci. Lett.*, *222*, 451–467.

Dixon, T., J. Decaix, F. Farina, K. Furlong, R. Malservisi, R. Bennett, F. Suarez-Vidal, J. Fletcher, and J. Lee (2002), Seismic cycle and rheological effects on estimation of present-day slip rates for the Agua Blanca and San Miguel-Vallecitos faults, northern Baja California, Mexico, *J. Geophys. Res.*, *107*(B10), 2226, doi:10.1029/2000JB000099.

Dixon, T. H., E. Norabuena, and L. Hotaling (2003), Paleoseismology and Global Positioning System: Earthquake-cycle effects and geodetic versus geologic fault slip rates in the eastern California shear zone, *Geology*, *31*, 55–58.

Du, Z., and G. R. Foulger (2001), Variation in the crustal structure across Iceland, *Geophys. J. Int.*, *145*, 246–264.

Dziewonski, A. M., G. Ekstroem, and N. N. Maternovskaya (2001), Centroid-moment tensor solutions for April–June 2000, *Phys. Earth Planet. Inter.*, *123*, 1–14.

Einarsson, P. (1991), Earthquakes and present-day tectonism in Iceland; Imaging and understanding the lithosphere of Scandinavia and Iceland, *Tectonophysics*, *189*, 261–279.

Einarsson, P., and K. Saemundsson (1987), Earthquake epicenters 1982–1985 and volcanic systems in Iceland, in *Í hlutarins eðli*, map, Menningarsjur, Reykjavk.

Einarsson, P., et al. (1993), The Iceland 1986 GPS geodetic survey: tectonic goals and data processing results, *Bull. Geod.*, *67*, 148–172.

Engeln, J. F., S. Stein, J. Werner, and R. G. Gordon (1988), Microplate and shear zone models for oceanic spreading center reorganizations, *J. Geophys. Res.*, *93*, 2839–2856.

Feigl, K. L., J. Gasperi, F. Sigmundsson, and A. Rigo (2000), Crustal deformation near Hengill Volcano, Iceland 1993–1998; coupling between magmatic activity and faulting inferred from elastic modeling of satellite radar interferograms, *J. Geophys. Res.*, *105*, 25,655–25,670.

Flóvenz, O. G., and K. Sæmundsson (1993), Heat flow and geothermal processes in Iceland, *Tectonophysics*, *225*, 123–138.

Foulger, G. R., Z. Du, and B. R. Julian (2003), Icelandic-type crust, *Geophys. J. Int.*, *155*, 567–590.

Garcia, S., N. O. Arnaud, J. Angelier, F. Bergerat, and C. Homberg (2003), Rift jump process in Northern Iceland since 10 Ma from $^{40}Ar/^{39}Ar$ geochronology, *Earth Planet. Sci. Lett.*, *214*, 529–544.

Gerke, K. (Ed.) (1974), *Crustal Movements in the Myvatn- and Thingvallavatn-Area, Both Horizontal and Vertical*, pp. 263–275, Springer, New York.

Govers, R. (1993), Dynamics of lithospheric extension: A modeling study, Ph.D. thesis, 240 pp, Utrecht Univ., Utrecht.

Gudmundsson, A. (1987), Tectonics of the Thingvellir fissure swarm, SW Iceland, *J. Struct. Geol.*, *9*, 61–69.

Gudmundsson, A. (2000), Dynamics of volcanic systems in Iceland: Example of tectonism and volcanism at juxtaposed hot spot and mid-ocean ridge systems, *Annu. Rev. Earth Planet. Sci.*, *28*, 107–140.

Hardarson, B. S., J. G. Fitton, R. M. Ellam, and M. S. Pringle (1997), Rift relocation: A geochemical and geochronological investigation of a palaeo-rift in northwest Iceland, *Earth Planet. Sci. Lett.*, *153*, 181–196.

Hey, R. (1977), A new class of pseudofaults and their bearing on plate tectonics: A propagating rift model, *Earth Planet. Sci. Lett.*, *37*, 321–325.

Hey, R., F. K. Duennebier, and J. W. Morgan (1980), Propagating rifts on mid-ocean ridges, *J. Geophys. Res.*, *85*, 3647–3658.

Hirth, G., and D. L. Kolhstedt (2004), Rheology of the upper mantle and the mantle wedge: A view from the experimentalists, in *Inside the Subduction Factory*, *Geophys. Monogr. Ser.*, vol. 138, edited by J. M. Eiler, pp. 83–106, AGU, Washington, D. C.

Hofton, M. A., and G. R. Foulger (1996), Postrifting anelastic deformation around the spreading plate boundary, north Iceland: 1. Modeling of the 1987–1992 deformation field using a viscoelastic Earth structure, *J. Geophys. Res.*, *101*, 25,403–25,421.

Hreinsdóttir, S., P. Einarsson, and F. Sigmundsson (2001), Crustal deformation at the oblique spreading Reykjanes Peninsula, SW Iceland; GPS measurements from 1993 to 1998, *J. Geophys. Res.*, *106*, 13,803–13,816.

Jóhannesson, H. (1989), Age of the Hallmundahraun lava flow in Borgarfjordur, *Fjolrit Natturufraedistofnunar*, *9*, 1–12.

Jóhannesson, H., S. P. Jakobson, and K. Sæmundsson (1990), Geological map of Iceland, sheet 6, South-Iceland, 3d ed., edited, Icelandic Mus. of Nat. Hist. and Icelandic Geod. Surv., Reykjavik.

Jónsson, S., P. Einarsson, and F. Sigmundsson (1997), Extension across a divergent plate boundary, the Eastern Volcanic rift zone, south Iceland, 1967–1994, observed with GPS and electronic distance measurements, *J. Geophys. Res.*, *102*, 11,913–11,929.

Karato, S., and P. Wu (1993), Rheology of the upper mantle: A synthesis, *Science*, *260*, 771–778.

Kirby, S. H. (1983), Rheology of the lithosphere, *Rev. Geophys.*, *21*, 1458–1487.

Kjartansson, G. (1964), Geological map of Iceland, sheet 5, central Iceland, Mus. of Nat. Hist., Dep. of Geol. and Geogr., Reykjavik.

LaFemina, P. C. (2005), Plate boundary zone deformation measured by GPS and implications for long-term geologic processes, Ph.D. thesis, 200 pp, Univ. of Miami, Rosenstiel Sch. of Mar. and Atmos. Sci., Miami, Fla.

Larsen, G. (1984), Recent volcanic history of the Veidivotn fissure swarm, southern Iceland: An approach to volcanic risk assessment, *J. Volcanol. Geotherm. Res.*, *22*, 33–58.

Linde, A. T., K. Agustsson, I. S. Sacks, and R. Stefánsson (1993), Mechanism of the 1991 eruption of Hekla from continuous borehole strain monitoring, *Nature*, *365*, 737–740.

Lippitsch, R., R. S. White, and H. Soosalu (2005), Precise hypocentre relocation of microearthquakes in a high-temperature geothermal field: The Torfajökull central volcano, Iceland, *Geophys. J. Int.*, *160*, 370–387.

MacDonald, K. C., and P. J. Fox (1983), Overlapping spreading centres: New accretion geometry on the East Pacific Rise, *Nature*, *302*, 55–58.

Malservisi, R., T. H. Dixon, P. C. La Femina, and K. P. Furlong (2003), Holocene slip rate of the Wasatch fault zone, Utah, from geodetic data: Earthquake cycle effects, *Geophys. Res. Lett.*, *30*(13), 1673, doi:10.1029/2003GL017408.

Mao, A., C. G. A. Harrison, and T. H. Dixon (1999), Noise in GPS coordinate time series, *J. Geophys. Res.*, *104*, 2797–2816.

Melosh, H. J., and A. Raefsky (1981), A simple and efficient method for introducing faults into finite element computations, *Bull. Seismol. Soc. Am.*, *71*, 1391–1400.

Meyer, P. S., H. Sigurdsson, and J.-G. Schilling (1985), Petrological and geochemical variations along Iceland's neovolcanic zones, *J. Geophys. Res.*, *90*, 10,043–10,072.

Mogi, K. (1958), Relations between the eruptions of various volcanoes and the deformations of the ground surfaces around them, *Bull. Earthquake Res. Inst. Univ. Tokyo*, *36*, 99–134.

Okada, Y. (1985), Surface deformation due to shear and tensile faults in a half-space, *Bull. Seismol. Soc. Am.*, *75*, 1135–1154.

Oskarsson, N., S. Steinthorsson, and G. E. Sigvaldason (1985), Iceland geochemical anomaly: origin, volcanotectonics, chemical fractionation, and isotope evolution of the crust, *J. Geophys. Res.*, *90*, 10,011–10,025.

Pagli, C., R. Pedersen, F. Sigmundsson, and K. L. Feigl (2003), Triggered fault slip on June 17, 2000 on the Reykjanes Peninsula, SW Iceland captured by radar interferometry, *Geophys. Res. Lett.*, *30*(6), 1273, doi:10.1029/2002GL015310.

Pedersen, R., and F. Sigmundsson (2004), InSAR based sill model links spatially offset areas of deformation and seismicity for the 1994 unrest episode at Eyjafjallajökull volcano, Iceland, *Geophys. Res. Lett.*, *31*, L14610, doi:10.1029/2004GL020368.

Pedersen, R., K. L. Feigl, S. Jónsson, T. Árnadóttir, and F. Sigmundsson (2001), Coseismic inferferograms of two Ms 6.6 earthquakes in the South Iceland seismic zone, June 2000, *Geophys. Res. Lett.*, *28*, 3341–3344.

Pedersen, R., F. Sigmundsson, K. L. Feigl, and T. Árnadóttir (2003), Fault slip distribution of two June 2000 M_w6.5 earthquakes in south Iceland estimated from joint inversion of InSAR and GPS measurements, *Earth Planet. Sci. Lett.*, *213*, 487–502.

Pollitz, F. F., and I. S. Sacks (1996), Viscosity structure beneath northeast Iceland, *J. Geophys. Res.*, *101*, 17,771–17,793.

Sæmundsson, K. (1974), Evolution of the axial rift zone in northern Iceland and the Tjornes Fracture Zone, *Geol. Soc. Am. Bull.*, *85*, 495–504.

Sæmundsson, K. (1992), Geology of the Thingvallavatn area, *Oikos*, *64*, 40–68.

Savage, J. C., and R. O. Burford (1973), Geodetic determination of relative plate motion in central California, *J. Geophys. Res.*, *78*, 832–845.

Sella, G. F., T. H. Dixon, and A. Mao (2002), REVEL: A model for Recent plate velocities from space geodesy, *J. Geophys. Res.*, *107*(B4), 2081, doi:10.1029/2000JB000033.

Sigmundsson, F. (1991), Post-glacial rebound and asthenosphere viscosity in Iceland, *Geophys. Res. Lett.*, *18*, 1131–1134.

Sigmundsson, F., and P. Einarsson (1992), Glacio-isostatic crustal movements caused by historical volume change of the Vatnajökull ice cap, Iceland, *Geophys. Res. Lett.*, *19*, 2123–2126.

Sigmundsson, F., and P. Einarsson (2000), 1994–2000 volcanic and seismic unrest at a 200-km-long stretch of the Mid-Atlantic Ridge plate boundary in Iceland: Episodic magma delivery, *Eos Trans. AGU*, *81*(48), Fall Meet. Suppl., Abstract T22A-17.

Sigmundsson, F., P. Einarsson, and R. Bilham (1992), Magma chamber deflation recorded by the Global Positioning System: the Hekla 1991 eruption, *Geophys. Res. Lett.*, *19*, 1483–1486.

Sigmundsson, F., P. Einarsson, R. Bilham, and E. Sturkell (1995), Rift-transform kinematics in South Iceland; deformation from Global Positioning System measurements, 1986 to 1992, *J. Geophys. Res.*, *100*, 6235–6248.

Sigmundsson, F., P. Einarsson, S. T. Rognvaldsson, G. R. Foulger, K. M. Hodgkinson, and G. Thorbergsson (1997), The 1994–1995 seismicity and deformation at the Hengill triple junction, Iceland; triggering of earthquakes by minor magma injection in a zone of horizontal shear stress, *J. Geophys. Res.*, *102*, 15,151–15,161.

Sigmundsson, F., R. Pedersen, K. L. Feigl, E. Sturkell, P. Einarsson, S. Jónsson, K. Agustsson, A. Linde, and F. Bretar (2001), Joint interpretation of geodetic data for volcano studies: Evaluation of pre- and co-eruptive deformation for the Hekla 2000 eruption from InSAR, tilt, GPS and strain data, *Eos Trans. AGU*, *82*(47), Fall Meet. Suppl., Abstract V21E-07.

Sigurdsson, H., and S. R. J. Sparks (1978), Lateral magma flow within rifted Icelandic crust, *Nature*, *274*, 126–130.

Stefánsson, R., et al. (1993), Earthquake prediction research in the south Iceland seismic zone and the SIL Project, *Bull. Seismol. Soc. Am.*, *83*, 696–716.

Stein, S., and R. G. Gordon (1984), Statistical tests of additional plate boundaries from plate motion inversions, *Earth Planet. Sci. Lett.*, *69*, 401–412.

Sturkell, E., F. Sigmundsson, and P. Einarsson (2003a), Recent unrest and magma movements at Eyjafjallajökull and Katla volcanoes, Iceland, *J. Geophys. Res.*, *108*(B8), 2369, doi:10.1029/2001JB000917.

Sturkell, E., F. Sigmundsson, P. Einarsson, H. Geirsson, and M. J. Roberts (2003b), Magma inflow into Katla, one of Iceland's most hazardous volcanoes, *Eos Trans. AGU*, *82*(47), Fall Meet. Suppl., Abstract V12G-07.

Tryggvason, E. (1968), Measurement of surface deformation in Iceland by precision leveling, *J. Geophys. Res.*, *73*, 7039–7050.

Tryggvason, E. (1982), Recent ground deformation in continental and oceanic rift zones, in *Continental and Oceanic Rifts*, *Geodyn. Ser.*, vol. 8, edited by G. Pálmason, pp. 17–29, AGU, Washington, D. C.

Tryggvason, E. (1990), Hoggun Almanagjar. Maelingar a Thingvollum 1990 (Displacement of Almannagja. Measurements at Thingvellir 1990), Nord. Volcanol. Inst., Reykjavik.

Tryggvason, E. (1994), Observed ground deformation at Hekla, Iceland prior to and during the eruptions of 1970, 1980–1981 and 1991: Internal structure of volcanoes and geophysical precursors of eruptions, *J. Volcanol. Geotherm. Res.*, *61*, 281–291.

Venzke, E., R. W. Wunderman, L. McClelland, T. Simkin, J. F. Luhr, L. Siebert, and G. Mayberry (2002), Global Volcanism, 1968 to the Present, *Digital Inf. Ser.*, *GVP-4*, Global Volcanism Program, Smithson. Inst., Washington, D. C. (Available at http://www.volcano.si.edu/gvp/reports/)

Walker, G. P. L. (1960), Zeolite zones and dyke distribution in relation to the structure of the basalts in Eastern Iceland, *J. Geol.*, *69*, 515–528.

Wessel, P., and W. H. F. Smith (1994), New version of generic mapping tools released, *Eos Trans. AGU*, *76*, 329.

Zumberge, J. F., M. B. Heflin, D. C. Jefferson, M. M. Watkins, and F. H. Webb (1997), Precise point positioning for the efficient and robust analysis of GPS data from large networks, *J. Geophys. Res.*, *102*, 5005–5017.

T. Árnadóttir, F. Sigmundsson, and E. Sturkell, Nordic Volcanological Center, Institute of Earth Sciences, University of Iceland, Sturlagata 7, Askja, IS-101 Reykjavik, Iceland.

T. H. Dixon and P. C. LaFemina, Rosenstiel School of Marine and Atmospheric Sciences, University of Miami, 4600 Rickenbacker Causeway, Miami, FL 33149, USA. (plafemina@rsmas.miami.edu)

P. Einarsson, Science Institute, University of Iceland, Dunhaga 3, IS-107 Reykjavik, Iceland.

R. Malservisi, Section Geophysics, Department of Geology and Environmental Sciences, Ludwig-Maximilians University, Theresienstr. 41, D-80333 Munich, Germany.